

Highlights

- Detailed stratigraphic record of the Paleocene-Eocene thermal maximum in shallow marine environment of the northern Indian margin, eastern Tethys ocean
- Two scenarios may be envisaged for the major origin of Paleocene/Eocene disconformity: tectonic or climatic control

1 **Shallow-water carbonate responses to the Paleocene–Eocene Thermal Maximum**
2 **in the Tethyan Himalaya (southern Tibet): tectonic and climatic implications**

3 Juan Li¹, Xiumian Hu^{1*}, Eduardo Garzanti², Marcelle BouDagher-Fadel³

4 *1 State Key Laboratory of Mineral Deposit Research, School of Earth Sciences and Engineering,*
5 *Nanjing University, Nanjing 210023, China*

6 *2 Laboratory for Provenance Studies, Department of Earth and Environmental Sciences,*
7 *Università di Milano-Bicocca, 20126 Milano, Italy*

8 *3 Department of Earth Sciences, University College London, London WC1H 0BT, UK*

9 **Corresponding author: Dr. Xiumian Hu*

10 *E-mail: huxm@nju.edu.cn; Tel: 0086 25 89683002*

11

12 **Abstract**

13 This study presents a detailed stratigraphic record of the Paleocene–Eocene Thermal
14 Maximum (PETM) in the Gamba area of the Tethyan Himalaya, a carbonate-platform succession
15 originally deposited along the southern margin of the eastern Tethys Ocean. The
16 Paleocene-Eocene boundary interval is marked by a negative carbon isotope excursion at the
17 boundary between members 3 and 4 of the Zongpu Formation. The succession is erosionally
18 truncated at this surface, which is overlain by an intraformational carbonate conglomerate, and
19 only the upper part of the PETM interval is preserved. Foraminiferal assemblages of Shallow
20 Benthic Zone 4 are present below the conglomerate bed, but are replaced by assemblages of

21 Shallow Benthic Zone 6 above the conglomerate. Depositional facies also change across this
22 surface; below the disconformity, floatstones and packstones containing nummulitid forams
23 record progressive transgression in an open-marine environment, whereas restricted or lagoonal
24 inner-ramp deposits containing *Alveolina* and *Orbitolites* are typical above the disconformity. The
25 prominent negative excursion observed in the $\delta^{13}\text{C}$ of whole-rock carbonate (-1.0‰ at Zongpu,
26 -2.4‰ at Zengbudong) and organic matter (-24.7‰, at Zengbudong) is correlated to the
27 characteristic PETM carbon isotope excursion. This major negative excursion in shallow-marine
28 carbonates may have partly resulted from syndepositional alteration of organic matter. The erosional
29 unconformity can be constrained to the lower PETM interval (between 56 and 55.5 Ma), and is
30 identifiable throughout the Tethyan Himalaya. This widespread disconformity is attributable to
31 tectonic uplift associated with the southward migration of an orogenic wave, originated 3 ± 1 Ma
32 earlier in the middle Paleocene at the first site of India-Asia continent-continent collision. A
33 possible eustatic component of the pre-PETM sea-level fall, which resulted in the excavation of
34 incised valleys filled during the subsequent sea-level rise when the conglomerate bed was
35 deposited, remains to be assessed.

36 **Key words:** PETM; Tethys Ocean; Carbonate platform; Disconformity; India-Asia collision;
37 Carbon isotope excursion

38

39 1. Introduction

40 The Paleocene–Eocene Thermal Maximum (PETM) was a geologically brief (~ 170-200 kyr)
41 episode of globally elevated temperatures (Röhl et al., 2007; Murphy et al., 2010), superimposed

42 on a longer-term late Paleocene to early Eocene warming trend, which culminated in the highest
43 ocean temperatures of the Cenozoic (the early Eocene climatic optimum; [Kennett and Stott, 1991](#);
44 [Zachos et al., 2001](#)). The PETM was characterized by global warming of both the earth's surface
45 and the deep oceans, by 5-8° C ([McInerney and Wing, 2011](#)). Its onset is defined by a negative
46 carbon isotope excursion (CIE) recorded worldwide ([Dupuis et al., 2003](#)). Although the ultimate
47 cause and trigger of the CIE is uncertain ([Sluijs et al., 2006](#)), the dissociation of methane hydrates
48 along continental margins is a plausible hypothesis that may explain the injection of large amounts
49 of ¹³C-depleted carbon into oceanic and atmospheric reservoirs ([Dickens et al., 1997](#)). Major
50 global biotic changes occurred simultaneously with the CIE, including a major extinction of
51 deep-sea benthic foraminifera, blooms of tropical and subtropical planktonic foraminifera, a
52 turnover in 'larger benthic foraminifera', an increased abundance of dinoflagellates, and the
53 disappearance of coral reefs ([Bowen et al., 2006](#); [Sluijs et al., 2007](#); [Speijer et al., 2012](#)). The
54 onset of the CIE is an excellent global chemostratigraphic correlation tool ([McInerney and Wing,](#)
55 [2011](#)), and is formally used to define the base of the Eocene ([Aubry et al., 2007](#)).

56 To fully understand biotic responses to climate change during the PETM, detailed analyses of
57 faunal and floral evolution are needed from a wide spectrum of different environments, including
58 the deep oceans, shallow seas, and terrestrial settings. Despite major advances in our
59 understanding of the PETM in open-marine environments, shallow-marine settings remain poorly
60 explored, and the effects of this global climatic event on the widespread epeiric carbonate
61 platforms of the Paleogene remain unclear. The Tethys Ocean was a vast, east-west trending
62 subtropical seaway during the Paleogene, with neritic deposition occurring in a variety of
63 environments along its margins, making it an excellent place to study the PETM in

64 shallow-marine settings.

65 The thick shallow-marine carbonate succession of the Tethyan Himalaya spans the critical
66 late Paleocene-early Eocene interval, and is characterized by abundant index fossils ([Willems et](#)
67 [al., 1993](#); [Hu et al., 2012](#); [Zhang et al., 2013](#); [Li et al., 2015](#)), offering a rare opportunity to study a
68 detailed, biostratigraphically controlled record of the PETM in the eastern Tethys. Biostratigraphy
69 based on larger benthic foraminifera, coupled with precise carbon isotope chemostratigraphy,
70 allows us to place firm constraints on the stratigraphic and environmental evolution of the Indian
71 margin during the very first stages of the India-Asia collision, a period that spans the critical
72 interval of the PETM.

73 **2. Geologic setting and lithostratigraphy**

74 The Tethyan Himalaya, situated between the Greater Himalaya to the south and the
75 Indus-Yarlung-Zangbo Suture and Lhasa Block to the north ([Fig. 1A](#)), consists of sedimentary
76 rocks originally deposited along the northern margin of the Indian continent. The Tethyan
77 Himalaya is traditionally subdivided into southern and northern zones, separated by the
78 Gyirong-Kangmar Thrust. The southern zone includes a Paleozoic to Eocene succession,
79 composed largely of shelf carbonates and terrigenous deposits ([Willems et al., 1996](#); [Sciunnach](#)
80 [and Garzanti, 2012](#)), whereas the northern zone is dominated by deeper-water Mesozoic to
81 Paleocene slope and rise sediments. Paleomagnetic data indicate that the Tethyan Himalaya was
82 located at peri-equatorial latitudes in the latest Mesozoic and early Cenozoic, ranging from
83 $5.6\pm 2.8^\circ$ S during Campanian-Maastrichtian time to $10.1\pm 2.0^\circ$ N during Selandian-Thanetian time
84 ([Yi et al., 2011](#)).

85 Our study area is located in the southern Tethyan Himalaya, near the town of Gamba (Fig.
86 1B). The site has a continuously exposed marine sedimentary succession ranging from the Upper
87 Cretaceous to Eocene, subdivided into three lithostratigraphic units (the Jidula, Zongpu and Enba
88 formations). Lower Paleocene shoreface deposits of the Jidula Formation consist of quartzose
89 sandstones derived from the Indian continent (Garzanti and Hu, 2015). The overlying Zongpu
90 Formation is composed of thin- to massively-bedded fossiliferous limestones at the base, with
91 nodular limestones in the middle and thick-bedded fossiliferous limestones in the upper part of the
92 formation (Willems and Zhang, 1996; Li et al., 2015). In the Gamba area, the Zongpu Formation
93 can be further subdivided into four members; thin- to medium-bedded limestones in member 1,
94 nodular limestones in member 2, nodular marly limestones in member 3, and thick- to
95 massively-bedded limestones in member 4. Members 3 and 4 are separated by a lenticular
96 conglomerate bed, marking an erosional disconformity that roughly corresponds to the
97 Paleocene-Eocene boundary (Wang et al., 2010; Wan et al., 2002; Li et al., 2015; Fig. 2B, 2C, 2D).
98 The Enba Formation comprises greenish-grey marls, intercalated in the upper part of the formation
99 with litho-quartzose sandstones sourced from the Asian continent, and deposited in prodelta to
100 offshore environments (Wan et al., 2002; Hu et al., 2012).

101 3. Materials and methods

102 3.1. Stratigraphic sections

103 We focused our study on the Zongpu Formation, by measuring two main sections in the
104 Gamba area (Zongpu and Zengbudong), and sampling them in detail for petrographic,
105 biostratigraphic and carbon isotope analysis (Fig. 1).

106 Microfacies analysis was carried out on 550 thin sections from the Zongpu section and 80
107 thin sections from the Zengbudong section using transmitted-light microscopy. This allowed us to
108 make semiquantitative estimates of the main sedimentary components, as well as observe primary
109 textural and diagenetic features, identify microfossils (with a special emphasis on larger benthic
110 foraminifera), and interpret of depositional settings. Samples for isotope measurements were
111 collected with an average spacing of 1 m, reduced to ~0.4 m across the Paleocene-Eocene
112 boundary. Biostratigraphic correlations were based on the distribution of larger benthic
113 foraminifera (identification based on [Hottinger, 1960](#); [BouDagher-Fadel, 2008](#)). We used the
114 Tethyan Shallow Benthic Zonation established by [BouDagher-Fadel \(2008, 2015\)](#). These shallow
115 benthic biozones can be correlated with the well-established ranges of planktonic foraminifera
116 ([BouDagher-Fadel, 2013](#)), in order to assign biostratigraphic ages to different intervals.

117 ***3.2. Carbon and oxygen isotopes***

118 To assemble a detailed chemostratigraphic record of the studied sections, we analyzed
119 whole-rock carbonate isotope values throughout the entire succession. We processed a total of 357
120 samples from the Zongpu section and 84 from the Zengbudong section. Powdered samples were
121 obtained by micro-drilling, taking care to avoid cement-filled veins and pores, or larger bioclasts.
122 The carbon and oxygen isotope ratios of powdered samples were measured at the State Key
123 Laboratory for Mineral Deposits Research at Nanjing University, using a Finnigan MAT Delta
124 Plus XP mass spectrometer coupled to an in-line GasBench II autosampler. Samples were reacted
125 with purified orthophosphoric acid at 70° C. Data are expressed in standard delta notation, as
126 permil deviations from the Vienna Pee Dee Belemnite (VPDB) standard. Duplicate measurements
127 of standards yielded an analytical precision (1σ) of 0.05‰ for $\delta^{13}\text{C}$ and 0.07‰ for $\delta^{18}\text{O}$.

128 To supplement our carbonate isotope results, we analyzed organic carbon isotopes across the
129 critical Paleocene-Eocene boundary interval in the Zengbudong section. Thirty-eight samples
130 were decarbonated using 10% HCl, and analysed at the SINOPEC Wuxi Research Institute of
131 Petroleum Geology, using a Finnigan MAT Delta Plus XL mass spectrometer. The results were
132 corrected to the VPDB scale and are expressed using delta notation. Additionally, 14 limestone
133 clasts collected from the conglomerate bed in the Zengbudong section were analyzed for both
134 whole-rock carbonate and organic carbon isotopes.

135 **4. Results**

136 *4.1. Lithostratigraphy*

137 The sedimentology and stratigraphy of the Zongpu and Zengbudong sections are described in
138 detail in [Li et al. \(2015\)](#). Here we focus on the stratigraphic interval immediately surrounding the
139 Paleocene-Eocene boundary, and on the sedimentological features of the Paleocene-Eocene
140 disconformity (Fig. 3).

141 Below the conglomerate bed, the uppermost strata of member 3 are composed mainly of
142 floatstones or packstones, which contain nummulitids. This interval records the progressive
143 transition to open-marine environments, with the uppermost strata deposited below fair-weather
144 wave base (Fig. 3C).

145 The ≤ 4 m thick conglomerate bed, found marking the boundary between members 3 and 4 of
146 the Zongpu Formation in the Gamba area, is markedly lenticular in shape, with a sharp erosional
147 base and flat, normally-graded top (Fig. 2A, 2E). Clasts are mostly subrounded to rounded, though
148 some angular clasts are present. They range in diameter from 0.5 to 15 cm, and consist mainly of

149 coarse-grained, nummulitid-bearing wackestones and packstones derived from the coeval (or
150 slightly older) Thanetian limestones of member 3 (Fig. 3B). The poor sorting, homogeneous
151 character of the clasts, and presence of some angular fragments suggests a local source area, and
152 possibly rapid transport and deposition. The occurrence of rounded clasts does imply some
153 transport in a channel system, but not to the same degree that would be inferred from rounded
154 silicate clasts, since limestone pebbles are rounded quite easily by mechanical abrasion (Kuenen,
155 1964; Mills, 1979). The lenticular bedding and erosive contact with underlying strata both indicate
156 deposition by bedload traction in a high energy, channelized flow. The thicker, more laterally
157 continuous conglomerate units are interpreted to have been deposited in an incised channel, within
158 a braided channel system (Wang et al., 2010; Li et al., 2015).

159 Above the conglomerate bed, the base of member 4 consists mainly of restricted to lagoonal
160 inner-ramp deposits, characterized by *Alveolina* and *Orbitolites*. These transition up-section into
161 shallow-marine deposits, and finally open-marine floatstones with *Nummulites* and *Alveolina*,
162 deposited below wave base in a middle ramp environment (Fig. 3A).

163 4.2. Biostratigraphy

164 The biostratigraphy of the Upper Cretaceous to lower Paleogene shallow-water succession of
165 the Tibetan Himalaya is described in detail in BouDagher-Fadel et al. (2015), which correlated the
166 planktonic foraminiferal zones of BouDagher-Fadel (2013) and the shallow benthic foraminiferal
167 zones of the Paleogene into a comprehensive new Tibetan biozonation scheme (Fig. 4). Here we
168 focus on: 1) the stratigraphic interval spanning the Paleocene-Eocene boundary, and 2) the
169 biostratigraphic features of the Paleocene-Eocene disconformity.

170 In both studied sections, the boundary between SBZ3 and SBZ4 (or TP2 and TP3) is defined
171 by the first appearance of *Aberisphaera gambanica*. Within SBZ4/TP3, *Lockhartia conditi*,
172 *Lockhartia haimei*, *Lockhartia cushmani*, *Daviesina langhami* (Fig. 5A), *Orbitosiphon*
173 *punjabensis* (Fig. 5B), *Ranikothalia sindensis* (Fig. 5C-a), *Orbitosiphon praepunjabensis* (Fig.
174 5C-b), *Miscellanea juliettae* (Fig. 5D), *Lockhartia roeae* (Fig. 5C-d) and *Miscellanea yvetteae* (Fig.
175 5E) are common. The first appearance of *Alveolina pasticillata* and *Alveolina ellipsoidalis* (Fig.
176 5F-b) marks the base of TP5 (within the lower part of SBZ6), corresponding to the base of the
177 Ypresian. This subzone is dominated by *Orbitolites complanatus* (Fig. 5F-a), *Glomalveolina*
178 *subtilis*, *Alveolina pasticillata*, *Alveolina ellipsoidalis* (Fig. 5H), *Alveolina aramaea* and *Alveolina*
179 *illerdensis*. The boundary between SBZ6 and SBZ7 is marked by the first appearance of *Alveolina*
180 *moussoulensis*.

181 Carbonate clasts from the conglomerate bed in the Gamba area yielded SBZ 4 to SBZ 6 index
182 fossils, including *Lockhartia haimei*, *Lockhartia conditi*, *Daviesina langhami*, *Miscellanea*
183 *juliettae* and *M. yvetteae* in SBZ4, *Alveolina vredenburgi* in SBZ5, and *Orbitolites complanatus*
184 and *Alveolina ellipsoidalis* in SBZ 6 (Fig. 3, Fig. 5G).

185 4.3. Stable carbon isotope stratigraphy

186 Stable carbon isotope values are plotted stratigraphically in Fig. 6 for the Zongpu section and
187 Fig. 7 for the Zengbudong section. The lower Thanetian is characterized by high variability in
188 whole-rock carbonate isotope values, while the upper Thanetian and lower Eocene show $\delta^{13}\text{C}_{\text{carb}}$
189 values centered around +2 ‰ and +1‰, respectively, with an abrupt negative shift at the
190 disconformable transition from open marine to restricted lagoonal deposits marked by the

191 conglomerate bed (Figs. 6, 7). Above this negative excursion, a recovery trend is evident in both
192 Zongpu and Zengbudong sections, beginning in the *Alveolina* packstone or floatstone at the base
193 of member 4. The negative excursion in $\delta^{13}\text{C}_{\text{carb}}$ begins at 314.6 m in the Zongpu section ($\delta^{13}\text{C}_{\text{carb}}$
194 = -1.0‰) and at 12.7 m in the Zengbudong section ($\delta^{13}\text{C}_{\text{carb}}$ = -2.4‰), and persists over an interval
195 of ~4 m in the Zongpu section, of ~5.4 m in the Zengbudong section. The magnitude of the CIE
196 reaches 3.4‰ in the Zongpu section, and 4.9‰ in the Zengbudong section.

197 The organic carbon isotope values measured across the Paleocene-Eocene boundary in the
198 Zengbudong section display a trend similar to the whole-rock carbonate record. In the upper part
199 of member 3, $\delta^{13}\text{C}_{\text{org}}$ ranges from -22.1‰ to -21.6‰, with an average value of -21.8‰ (Fig. 7).
200 An abrupt negative excursion, with a magnitude of 3‰, occurs at the base of member 4 (-24.6‰).
201 These ^{13}C -depleted values persist over a 5.4 m interval, then show a positive trend corresponding
202 to that seen in carbonate isotopes, with values rising from -24.7‰ to -22.4‰.

203 The carbonate clasts in the conglomerate bed marking the Paleocene-Eocene boundary in the
204 Zengbudong section are apparently altered, and display extreme $\delta^{13}\text{C}_{\text{carb}}$ values, ranging from -2.4‰
205 down to -6‰ (Fig. 8A). The organic carbon isotope values of the carbonate range vary from -23.0 ‰
206 to -25.1‰ (Fig. 8B).

207 **5. The Paleocene–Eocene thermal event in the Himalaya**

208 Previous studies of shallow-water successions in the Pyrenean Basin in Spain
209 ([Orue-Etxebarria et al., 2001](#); [Pujalte et al., 2003, 2009, 2014, 2015, 2016](#)), the Galala Mountains
210 in Egypt ([Scheibner et al., 2005](#); [Scheibner and Speijer, 2009](#)), the Adriatic carbonate platform in
211 SW Slovenia ([Zamagni et al., 2008, 2012](#)), the Indus Basin in Pakistan ([Afzal et al., 2011](#)), the

212 Zagros Basin in SW Iran ([Bagherpour and Vaziri, 2012](#)), and the Pacific region ([Robinson, 2011](#)),
213 have extensively documented the correlation between the negative carbon isotope excursion
214 associated with the PETM and the evolution of larger benthic foraminifera. However, many of
215 these studies were conducted in European and Mediterranean regions corresponding to the western
216 Tethys; the applicability of Shallow Benthic Zones (SBZ) and regional biostratigraphic
217 correlations to the shallow-water environments of the eastern Tethys remains uncertain ([Wang et
218 al., 2010](#)), although [Zhang et al. \(2013\)](#) proposed a temporal correlation between the PETM and
219 the evolution of larger benthic foraminifera in southern Tibet.

220 *5.1. Diagenetic effects on carbon isotope curves*

221 Dissolution and recrystallization processes during diagenesis of carbonate minerals can
222 significantly alter their carbon isotope composition ([Garzzone et al., 2004](#)). The carbon isotope
223 ratio of authigenic carbonate may also change as a result of the transformation of aragonite and
224 high-Mg calcite to low-Mg calcite during diagenesis, or from the presence of skeletal grains,
225 which may exhibit nonequilibrium isotopic fractionation ([Immenhauser et al., 2002](#); [Swart and
226 Eberli, 2005](#)). Thin section analysis reveals that the carbonates of the Zongpu Formation are
227 wackestones or packstones, with a homogeneous micritic matrix and skeletal grains. Microsparry
228 calcite is rare, and sparry calcite is absent, indicating that the original sedimentary fabric has been
229 largely preserved. The skeletal grains include both smaller and larger benthic foraminifera and
230 echinoderms, and were originally composed of low-Mg to high-Mg calcite. Mineralogical
231 stabilization of high-Mg calcite to low-Mg calcite can occur without any textural change in
232 skeletal calcite, especially in porcellanaceous foraminifera like alveolinids and larger miliolids
233 ([Budd and Hiatt, 1993](#)). In the absence of subaerial exposure, the transformation of high-Mg to

234 low-Mg calcite occurs under the influence of marine pore waters, with only minor modification of
235 the carbon isotope composition of skeletal grains. Overall, petrographic features suggest that
236 carbonate strata in the studied sections have undergone minimal diagenetic alteration.

237 Measured $\delta^{13}\text{C}$ values range from -4.0‰ to 2.5‰, and $\delta^{18}\text{O}$ values range from -10 ‰ to -4‰.
238 A crossplot of carbon and oxygen isotope values shows no significant correlation ($R^2=0.39$ for the
239 Zongpu section; $R^2=0.02$ for the Zengbudong section; Fig. 8A). The crossplot also lacks the slope
240 characteristic of “mixing lines” produced by the addition of variable quantities of cement to
241 primary skeletal calcite (Marshall, 1992), suggesting that the isotopic values obtained from the
242 studied sections likely record a primary palaeoceanographic signal.

243 *5.2. Completeness of the PETM record in southern Tibet*

244 The onset of the CIE and its shape are considered to be the most reliable correlation tools for
245 the Paleocene-Eocene boundary interval (Röhl et al., 2007). The major environmental and biotic
246 changes associated with the PETM provide additional criteria to both pinpoint the
247 Paleocene-Eocene boundary and assess the stratigraphic completeness of the PETM event as
248 recorded in south Tibet.

249 In both studied sections of the Zongpu Formation, sedimentological and biostratigraphic
250 analyses indicate a major erosional unconformity between the top of member 3 (which dates to the
251 latest Paleocene SBZ 4), and the base of member 4 (which dates to the early Ypresian SBZ 6).
252 This disconformity should thus represent at least 400 kyr, corresponding to the missing SBZ5 and
253 the earliest part of SBZ6 (BouDagher-Fadel et al., 2008; Fig. 4). Analysis of carbonate clasts
254 contained in the conglomerate bed helps to further constrain the time interval represented by the

255 disconformity, and to assess the processes driving this erosion. Intraformational carbonate clasts
256 include index fossils from SBZ4 through SBZ6 (Fig. 3). The sedimentary record of the
257 Paleocene-Eocene boundary within SBZ6 (BouDagher-Fadel et al.,2008), including the onset of
258 the PETM, was thus truncated by latest Paleocene erosion.

259 The discontinuity of the sedimentary record is highlighted by the abruptness of the isotopic
260 excursion. In southern Tibet, the negative $\delta^{13}\text{C}_{\text{carb}}$ and $\delta^{13}\text{C}_{\text{org}}$ excursions are extremely sharp (from
261 2.5 to - 2.0‰ and from -21.6 to -24.6‰, respectively), consistent with the presence of a hiatus.
262 The base of the Eocene in the Gamba area also shows a sudden change from open marine to
263 restricted-lagoonal environments. Both $\delta^{13}\text{C}_{\text{carb}}$ and $\delta^{13}\text{C}_{\text{org}}$ values remain consistent or increase
264 slightly immediately below the conglomerate bed, implying that the onset of the CIE is not
265 recorded in these strata. The 4 to 7 m thick interval with consistently low $\delta^{13}\text{C}_{\text{carb}}$ and $\delta^{13}\text{C}_{\text{org}}$ values
266 (i.e., the CIE) is followed by a gradual return to pre-excursion values (Figs. 6, 7, 9), suggesting that
267 while the onset of the PETM is truncated by erosion, the stratigraphic record of the upper PETM
268 interval is expanded and continuous.

269 *5.3. Comparison between southern Tibet and other marine successions*

270 Constraining the magnitude of the CIE is critical to evaluating its potential causes (Higgins
271 and Schrag, 2006) and understanding the sensitivity of the climate system to the associated
272 greenhouse gas forcing. Measurements vary widely, ranging from 2‰ to 4.5‰ in marine
273 carbonates depending on the studied location and substrate (Giusberti et al., 2007; Sluijs and
274 Dickens, 2012). The observed magnitude of the negative excursion in our whole-rock carbonate
275 records (~3.4‰ in the Zongpu section and ~4.9 ‰ in the Zengbudong section) is slightly greater than

276 the values reported from other shallow-marine continental margins (e.g., between 2.8‰ and 3.5‰ for
277 the North American shelf; [John et al., 2008](#)), the Adriatic carbonate platform (~1‰ in the Kozina
278 section and ~3‰ in the Čebulovica section; [Zamagni et al., 2012](#)), Pacific guyots (~3‰; [Robinson,
279 2011](#)), and deep-sea bulk carbonates (between 2.5‰ and 4.0‰).

280 The magnitude of the negative CIE in our shallow-marine carbonate record is quite large
281 compared to open-marine records of the PETM, with an excursion in whole-rock carbonate samples of
282 up to 4.9‰ in the Zengbudong section ([Fig. 10](#)). The low $\delta^{13}\text{C}$ values of these carbonates may be due
283 to a combination of several effects, including restricted circulation and a smaller carbon reservoir size
284 in the platform-top water mass, a local flux of carbon weathering from the land, and syndepositional
285 diagenesis of carbonate mud in organic-rich sediments ([Immenhauser et al., 2008](#)).

286 In the Gamba area, the Zongpu Formation was deposited in a carbonate ramp setting characterized
287 by good water circulation, suggesting that water mass restriction was not a major factor. Low pore
288 water $\delta^{13}\text{C}$ values may have resulted from the oxidation of organic matter. Syndepositional dissolution
289 of CaCO_3 caused by organic matter oxidation can alter the isotopic composition of carbonate, resulting
290 in lower $\delta^{13}\text{C}$ values in diagenetic carbonates ([Sanders, 2003](#); [Patterson and Walter, 1994](#)). The
291 strongly negative excursions in whole-rock $\delta^{13}\text{C}_{\text{carb}}$ values observed in the Zongpu Formation may
292 reflect syndepositional alteration of organic matter. Climatic conditions during the PETM, with
293 intensified chemical weathering and seasonality driving more efficient physical weathering and erosion
294 ([Egger et al., 2005](#); [Giusberti et al., 2007](#)), promoted the accumulation of organic-rich black shales
295 along the margin of the Neo-Tethys Ocean ([Speijer and Wagner, 2002](#)). Current-driven redistribution
296 of organic matter along the carbonate ramp may have contributed to the differences in the magnitude of
297 negative carbon isotope excursions observed between the Zongpu and Zengbudong sections, with the

298 former characterized by less negative $\delta^{13}\text{C}_{\text{carb}}$ values.

299 **6. Origin of the P-E boundary unconformity**

300 The channelized intraformational conglomerate bed that marks the boundary between
301 members 3 and 4 of the Zongpu Formation in the Gamba area has long been biostratigraphically
302 correlated with a similar unit in the Zanskar Range of the northwestern Tethyan Himalaya. This
303 conglomerate is interpreted to be the result of tectonic uplift, due to landward migration of a
304 collision-related flexural wave (Garzanti et al., 1987). The same mechanism has been proposed to
305 explain the conglomerate bed in the Gamba area (Zhang et al., 2012; Li et al., 2015), and a similar
306 disconformity and conglomerate bed can be observed in the Tingri and Düela areas (unpublished
307 field observations). The Paleocene-Eocene erosional unconformity is not limited to the Gamba
308 area, but can be traced for 200 km across southern Tibet. Considering the similarity between
309 stratigraphic records in the Gamba area and the Zanskar Range, we conclude that this
310 Paleocene-Eocene disconformity is a widespread, roughly synchronous feature in the Tethyan
311 Himalaya. The combination of biostratigraphy and detailed carbon isotope chronostratigraphy
312 presented in this study allow us to establish that this erosional event occurred during the lower
313 PETM interval (i.e., around 56 or 55.5 Ma; Hilgen et al., 2010; Westerhold et al., 2012).

314 The origin of the Paleocene-Eocene boundary unconformity in the Tethyan Himalaya is
315 discussed below, in relation to: 1) tectonic uplift of the Zongpu carbonate platform, and 2)
316 climate-driven incision and erosion prior to the PETM.

317 **6.1. Tectonic uplift of the Zongpu platform**

318 Based on evidence from the northwestern Himalaya, Garzanti et al. (1987) proposed that the

319 Indian passive margin was tectonically uplifted by southward migration of an orogenic wave that
320 initiated at the Trans-Himalayan Trench during the onset of the collision between India and Asia.
321 In depositional settings from the outer Indian margin, exposed in the Zaskar Range, pelagic
322 outer-shelf sediments yielding planktonic foraminifera of Thanetian age are unconformably
323 overlain by peritidal dolostones and nummulitid-rich calcarenite shoals of early Ypresian age.
324 Channelized quartz-rich sandstone beds are reported to occur during the same interval in the inner
325 Zaskar margin (Nicora et al., 1987), whereas debris-flow conglomerates containing limestone
326 pebbles of Cretaceous to latest Paleocene age occur in the most distal part of the Indian margin
327 (Fuchs and Willems, 1990).

328 In the Gamba sections of southern Tibet, the unusually low carbon isotope values of
329 conglomerate clasts ($\delta^{13}\text{C}$ as negative as -6‰ PDB; Fig. 8) suggest a period of weathering and
330 freshwater influx associated with prolonged subaerial exposure (Immenhauser et al., 2002). This
331 interpretation is strongly supported by three independent lines of evidence: 1) the presence of
332 channelized intraformational conglomerates mantling a major stratigraphic disconformity; 2) a
333 stratigraphic gap of ~ 400 kyr, corresponding to the missing SBZ5; and 3) a sharp break in the
334 $\delta^{13}\text{C}_{\text{carb}}$ record, documented in all studied sections. Facies analysis, biostratigraphy, and carbon
335 isotope measurements thus provide compelling evidence that, during a period of warm climate and
336 sea level rise (Kominz et al., 2008; Sluijs et al., 2008), the Paleocene-Eocene disconformity was
337 produced via tectonic uplift. Collision with Asia was already underway (DeCelles et al., 2014; Hu
338 et al., 2015), and this marked uplift event recorded throughout the inner Tethyan Himalaya, from
339 Zaskar to southern Tibet, may be the result of an orogenic wave propagating from the point of
340 first continent-continent contact and moving progressively landward across the Indian margin.

341 Integrated biostratigraphic and zircon chronostratigraphic studies conducted on sedimentary
342 successions from the most distal part of the Indian margin indicate that the onset of collision
343 occurred in the Selandian (middle Paleocene) at 59 ± 1 Ma (DeCelles et al., 2014; Wu et al., 2014;
344 Hu et al., 2015). If the unconformity was indeed caused by tectonic uplift related to a flexural
345 wave, we can estimate the time required for the orogenic front to reach the inner Indian margin in
346 Gamba, Tingri and Zanskar to be 3 ± 1 Myr. Assuming an original paleomargin width between 250
347 and 300 km (van Hinsbergen et al., 2012; Lippert et al., 2014), this corresponds to a migration
348 velocity of 90 ± 20 km/Myr (mm/a). The convergence rate between India and Asia is estimated to
349 have been ~ 150 mm/a based on paleomagnetic data (Copley et al., 2010; van Hinsbergen et al.,
350 2011). A convergence/shortening ratio of 1.7 ± 1.0 is somewhat larger than what is typically
351 observed in orogenic belts generated by continental collision, but with all of the uncertainties
352 considered, it is still compatible with existing models (Doglioni et al., 2007).

353 **6.2. Climate-driven incision and erosion prior to the PETM**

354 It is widely understood that valleys in marine-basin margins are usually incised during
355 periods of relative sea-level fall, and filled with sediments during the subsequent sea-level rise
356 (Boyd et al., 2006; Strong and Paola, 2008; Pujalte et al., 2015). A sea-level lowstand preceding
357 the PETM has been widely recognized; in the Pyrenees (Pujalte et al., 2014, 2015, 2016), the
358 North Sea region (Dupuis, 2000), the Austrian Alps (northern margin of the Tethys, Egger et al.,
359 2009, 2011), and the Nile Valley (southern margin of the Tethys, Aubry, 2009). This sea level fall
360 was followed by an equally widespread sea-level rise.

361 In the Gamba area of the Tethyan Himalaya, the channelized intraformational conglomerate

362 bed within the Paleocene-Eocene boundary interval of the Zongpu Formation also marks the
363 boundary between the open-marine environments of member 3 and the restricted to lagoonal
364 inner-ramp deposits of member 4. The roughly coeval disconformity in the Zanskar Range
365 ([Garzanti et al., 1987](#)) clearly records a pronounced fall in relative sea-level, and consequently the
366 formation of an incised valley in previously deposited carbonate-ramp strata ([Li et al., 2015](#)). The
367 subsequent rise in relative sea-level began ~40 kyr before the Paleocene–Eocene boundary,
368 leading to the filling of incised valleys and deposition of the conglomerate bed. Relative sea-level
369 continued to rise during and after the PETM, leading to the deposition of floatstones containing
370 *Alveolina* and *Orbitolites* in member 4 of the Zongpu Formation. Deposition of the conglomerate
371 bed, which sedimentological evidence suggests may have occurred in a fluvio-deltaic or
372 shallow-marine environment, would have had to have been rapid in this scenario.

373 The tectonic and eustatic components of base-level change cannot be easily distinguished in
374 the stratigraphic record, and we are unable to deconvolve their relative contributions to the
375 formation of the Paleocene-Eocene disconformity. The unique features of the conglomerate bed,
376 which has no equivalent in the underlying Paleocene succession, point to a single specific event
377 driving subaerial exposure and erosion. Tectonic activity was certainly underway during these
378 earliest stages of the India-Asia collision, and therefore tectonic reduction of accommodation space
379 remains a viable explanation. This is especially true of the disconformity in the Zanskar region,
380 which separates pelagic marly limestones below from peritidal carbonates above, suggesting a
381 drastic relative sea-level fall of at least 100 meters. Glacio-eustasy is a mechanism capable of
382 driving large and rapid fluctuations in sea-level, but can be ruled out due to the extremely warm
383 climatic conditions around the Paleocene-Eocene boundary. The aquifer-eustasy hypothesis

384 (Wendler and Wendler, 2015) has yet to be proven as a workable alternative mechanism. However,
385 we have no evidence to rule out a climatically-driven eustatic component, and further work is
386 needed to better understand the possibly superimposed processes that drove deep incision and
387 erosion along the inner margin of the Tethyan Himalaya prior to the PETM.

388 7. Conclusions

389 This study reports a detailed stratigraphic record of the Paleocene–Eocene Thermal
390 Maximum from the Tethyan Himalaya. The succession is truncated by a major disconformity
391 around the Paleocene-Eocene boundary, marked by a conglomerate bed now identified in both the
392 Gamba and Tingri areas of southern Tibet. As a result of this unconformity, only the upper part of
393 the PETM interval is preserved. By coupling sedimentological, biostratigraphic, and geochemical
394 data, we were able to reconstruct in detail the sedimentary and tectonic evolution of the southern
395 Indian margin during the earliest stages of the India-Asia collision. Our results allows us to
396 conclude that:

397 1) The Paleocene-Eocene unconformity corresponds with the boundary between members 3
398 and 4 of the Zongpu Formation, documenting an abrupt environmental change from open-marine
399 environments below to restricted or lagoonal inner-ramp environments above. The prominent
400 negative excursion in $\delta^{13}\text{C}$ at the base of member 4 is seen in both whole-rock carbonate and
401 organic carbon records, and can correlated using larger-benthic-foraminifera biostratigraphy with
402 the carbon isotope excursion defining the PETM. The strong ^{13}C depletion seen in shallow-marine
403 carbonates in southern Tibet may have resulted partly from syndepositional alteration of organic
404 matter.

405 2) The marked negative shift in carbon isotope values across the Paleocene-Eocene boundary
406 is associated with conglomerate beds in the Gamba area of southern Tibet, and a stratigraphic gap
407 of as much as 400 kyr, providing compelling evidence of subaerial exposure. This major
408 Paleocene-Eocene disconformity may be ascribed to tectonic uplift associated with the southward
409 migration of an orogenic wave that originated 3 ± 1 Myr earlier, as India began to collide with Asia
410 in the middle Paleocene. Eustatic sea-level fall may have caused the incision of valleys prior to the
411 PETM, with subsequent filling of the valleys during the interval of conglomerate deposition,
412 however the impact of eustasy on the stratigraphy of the Tethyan Himalaya requires further study.

413 **Acknowledgments**

414 We would like to express our gratitude to Wei An, Zhong Han, and Mingyuan Lai for their
415 assistance in the field and the laboratory for Provenance Studies, and to Carlo Doglioni, Shijun
416 Jiang, Yongxiang Li and Jiangang Wang for their advice in preparing this manuscript. This study
417 was financially supported by the National Natural Science Fund for Distinguished Young Scholars
418 (41525007) and the Chinese MOST 973 Project (2012CB822001). We would also like to thank
419 our two reviewers and Editor Prof. Isabel Patricia Montanez for their constructive comments.

420 **References**

- 421 Afzal, J., Williams, M., Leng, M.J., Aldridge, R.J., Stephenson, M.H., 2011. Evolution of Paleocene to
422 Early Eocene larger benthic foraminifer assemblages of the Indus Basin, Pakistan. *Lethaia* 44,
423 299-320.
- 424 Aubry, M. P., Ouda, K., Dupuis, C., Berggren, W. A., Couvering, J. A. V., 2007. The Global Standard
425 Stratotype-section and Point (GSSP) for the base of the Eocene Series in the Dababiya section
426 (Egypt). *Episodes*, 30(4), 271.
- 427 Aubry, M.P., Dupuis, C., Berggren, W.A., Ouda, K., Knox, K., Sabour, A.A., 2009. Sea-level changes

428 bracket the PETM. In: Strong, P., Crouch, E., Hollis, C. (Eds.), and Biotic Events of the
429 Paleogene, CBEP 2009, Wellington, New Zealand, Conference program and Abstracts, p. 144

430 Bagherpour, B., Vaziri, M.R., 2012. Facies, paleoenvironment, carbonate platform and facies changes
431 across Paleocene Eocene of the Taleh Zang Formation in the Zagros Basin, SW-Iran. *Historical*
432 *Biology*, v. 24, p.121-142.

433 BouDagher-Fadel, M.K., Price, G.D., Hu, X., Li, J., 2015. Late Cretaceous to early Paleogene
434 foraminiferal biozones in the Tibetan Himalayas, and a pan-Tethyan foraminiferal correlation
435 scheme. *Stratigraphy*, v. 12, p. 67-91.

436 BouDagher-Fadel, MK, (2008). Evolution and Geological Significance of Larger Benthic Foraminifera:
437 Developments in Paleontology and Stratigraphy, Volume 21: Amsterdam, Elsevier, 540 p.

438 BouDagher-Fadel, MK, (2013). Biostratigraphic and geological significance of planktonic foraminifera,
439 2nd edition. London: OUP University College of London, 307 p

440 Bowen, G. J., Bralower, T. J., Delaney, M. L., Dickens, G. R., Kelly, D. C., Koch, P. L., et al., 2006,
441 Eocene hyperthermal event offers insight into greenhouse warming: EOS, Transactions, American
442 Geophysical Union, v. 87, p. 165-169.

443 Berggren, W.A., 1995. A revised Cenozoic geochronology and chronostratigraphy. Boyd, R., Dalrymple,
444 R. W., and Zaitlin, B. A., 2006. Estuarine and Incised-Valley Facies Models, in: *Facies Models*
445 *Revisited*, edited by: Posamentier, H.W. and Walker, R. G., SEPM Sp. Pub., v84, p 171–235.

446 Budd, A.D., and Hiatt, E.E., 1993, Mineralogical stabilization of high-magnesium
447 calcite—Geochemical evidence for intracrystal recrystallization within Holocene porcellaneous
448 foraminifera: *Journal of Sedimentary Petrology*, v. 63, p. 261–274

449 Copley, A., Avouac, J. P., and Royer, J. Y., 2010, India-Asia collision and the Cenozoic slowdown of
450 the Indian plate: Implications for the forces driving plate motions: *Journal of Geophysical*
451 *Research: Solid Earth* (1978–2012), v. 115, no. B3.

452 DeCelles, P., Kapp, P., Gehrels, G., and Ding, L., 2014, Paleocene-Eocene foreland basin evolution in
453 the Himalaya of southern Tibet and Nepal: Implications for the age of initial India-Asia collision:
454 *Tectonics*, v. 33, no. 5, p. 824-849.

455 Dickens, G. R., Castillo, M. M., and G. Walker, J. C., 1997, A blast of gas in the latest Paleocene:
456 Simulating first-order effects of massive dissociation of oceanic methane hydrate: *Geology*, v. 25,

457 no. 3, p. 259-262.

458 Doglioni, C., Carminati, E., Cuffaro, M., and Scrocca, D., 2007, Subduction kinematics and dynamic
459 constraints: *Earth-Science Reviews*, v. 83, no. 3, p. 125-175.

460 Dupuis, C., Aubry, M. P., Steurbaut, E., Berggren, W. A., Ouda, K., Magioncalda, R., and
461 Heilmann-Clausen, C., 2003. The Dababiya Quarry Section: Lithostratigraphy, clay mineralogy,
462 geochemistry and paleontology. *Micropaleontology*, 49(Suppl 1), 41-59.

463 Egger, H., 2011. The early Paleogene history of the Eastern Alps. In: Egger, H. (Ed.), *Climate and
464 Biota of the Early Paleogene, Field-Trip Guidebook, Salzburg, Austria. Berichte der Geologischen
465 Bundesanstalt*, v.86, p. 9–16.

466 Egger, H., Heilmann-Clausen, C., Schmitz, B., 2009. From shelf to abyss: record of the
467 Paleocene/Eocene boundary in the Eastern Alps (Austria). *Geol. Acta*, v7, p. 215–227.

468 Egger, H., Homayoun, M., Huber, H., Rögl, F., and Schmitz, B., 2005, Early Eocene climatic, volcanic,
469 and biotic events in the northwestern Tethyan Untersberg section, Austria: *Palaeogeography,
470 Palaeoclimatology, Palaeoecology*, v. 217, no. 3-4, p. 243-264.

471 Fuchs, G., and Willems, H., 1990, The final stages of sedimentation in the Tethyan Zone of Zanskar
472 and their geodynamic significance (Ladakh-Himalaya): *Jahrb. Geol. Bundesanstalt*, v. 133, p.
473 259-273.

474 Garzanti, E., and Hu, X., 2015, Latest Cretaceous Himalayan tectonics: Obduction, collision or
475 Deccan-related uplift?: *Gondwana Research*, v. 28, no. 1, p. 165-178.

476 Garzanti, E., Baud, A., Mascle, G., 1987. Sedimentary record of the northward flight of India and its
477 collision with Eurasia (Ladakh Himalaya, India). *Geodinamica Acta*, 1, 297-312.

478 Garzzone, C. N., Dettman, D. L., Horton, B. K., 2004. Carbonate oxygen isotope paleoaltimetry:
479 evaluating the effect of diagenesis on paleoelevation estimates for the Tibetan plateau.
480 *Palaeogeography, Palaeoclimatology, Palaeoecology*, 212(1), 119-140.

481 Giusberti, L., Rio, D., Agnini, C., Backman, J., Fornaciari, E., Tateo, F., and Oddone, M., 2007, Mode
482 and tempo of the Paleocene-Eocene thermal maximum in an expanded section from the Venetian
483 pre-Alps: *Geological Society of America Bulletin*, v. 119, no. 3-4, p. 391-412.

484 Higgins, J. A., and Schrag, D. P., 2006, Beyond methane: Towards a theory for the Paleocene–Eocene

485 Thermal Maximum: *Earth and Planetary Science Letters*, v. 245, no. 3-4, p. 523-537.

486 Hilgen, F. J., Kuiper, K. F., and Lourens, L. J., 2010, Evaluation of the astronomical time scale for the
487 Paleocene and earliest Eocene: *Earth and Planetary Science Letters*, v. 300, no. 1, p. 139-151.

488 Hottinger, L., 1960. Uber Eocene und Paleocene Alveolinen. *Eclogae Geol Helv*, v. 53, p. 265–283

489 Hu, X., Garzanti, E., Moore, T., and Raffi, I., 2015, Direct stratigraphic dating of India-Asia collision
490 onset at the Selandian (middle Paleocene, 59 ± 1 Ma): *Geology*, v. 43, no. 10, p. 859-862.

491 Hu, X., Sinclair, H. D., Wang, J., Jiang, H., and Wu, F., 2012, Late Cretaceous-Palaeogene stratigraphic
492 and basin evolution in the Zhepure Mountain of southern Tibet: implications for the timing of
493 India-Asia initial collision: *Basin Research*, v. 24, no. 5, p. 520-543.

494 Immenhauser, A., Holmden, C., and Patterson, W. P., 2008, Interpreting the carbon isotope record of
495 ancient shallow epeiric seas: lessons from the recent: *Geological Association of Canada Special
496 Paper*, v. 48, p. 137-174.

497 Immenhauser, A., Kenter, J. A., Ganssen, G., Bahamonde, J. R., Van Vliet, A., and Saher, M. H., 2002,
498 Origin and significance of isotope shifts in Pennsylvanian carbonates (Asturias, NW Spain):
499 *Journal of Sedimentary Research*, v. 72, no. 1, p. 82-94.

500 John, C. M., Bohaty, S. M., Zachos, J. C., Sluijs, A., Gibbs, S., Brinkhuis, H., and Bralower, T. J., 2008,
501 North American continental margin records of the Paleocene-Eocene thermal maximum:
502 Implications for global carbon and hydrological cycling: *Paleoceanography*, v. 23, no. 2, p. 1-20.

503 Kennett, J. P., and Stott, L. D., 1991, Abrupt deep sea warming palaeoceanographic changes and
504 benthic extinctions at the Palaeocene: *Nature*, v. 353, no. 6341, p. 225-229.

505 Kominz, M. A., Browning, J. V., Miller, K. G., Sugarman, P. J., Mizintseva, S., and Scotese, C. R.,
506 2008, Late Cretaceous to Miocene sea-level estimates from the New Jersey and Delaware coastal
507 plain coreholes: an error analysis: *Basin Research*, v. 20, no. 2, p. 211-226.

508 Kuenen, P. H., 1964. Experimental abrasion: 6. surf action. *Sedimentology*, v. 3, no.1, 29-43.

509 Li, J., Hu, X., Garzanti, E., An, W., and Wang, J., 2015, Paleogene carbonate microfacies and sandstone
510 provenance (Gamba area, South Tibet): Stratigraphic response to initial India–Asia continental
511 collision: *Journal of Asian Earth Sciences*, v. 104, p. 39-54.

512 Marshall, J. D., 1992, Climatic and oceanographic isotopic signals from the carbonate rock record and

513 their preservation: *Geol. Mag.* v. 129, no. 2, p. 143-160.

514 McInerney, F.A., Wing, S.L., 2011. The Paleocene-Eocene Thermal Maximum: A Perturbation of
515 Carbon Cycle, Climate, and Biosphere with Implications for the Future, *Annual Review of Earth
516 and Planetary Sciences*, Vol 39, pp. 489-516.

517 Mills, H. H., 1979. Downstream rounding of pebbles: a quantitative review. *Journal of Sedimentary
518 Research*, 49(1), 295-302.

519 Murphy, B.H., Farley, K.A., Zachos, J.C., 2010. An extraterrestrial ^3He -based timescale for the
520 Paleocene–Eocene thermal maximum (PETM) from Walvis Ridge, IODP Site 1266. *Geochimica
521 et Cosmochimica Acta*, 74(17): 5098-5108.

522 Nicora, A., Garzanti, E., and Fois, E., 1987, Evolution of the Tethys Himalaya continental shelf during
523 Maastrichtian to Paleocene (Zanskar, India): *Riv. It. Paleont. Strat.*, v. 92, p. 439-496.

524 Orue-Etxebarria, X., Pujalte, V., Bernaola, G., Apellaniz, E., Baceta, J. I., A. Payros, Nun ez-Betelu,
525 K., Serra-Kiel, J., and Tosquella, J., 2001, Did the Late Paleocene thermal maximum affect the
526 evolution of larger foraminifers? Evidence from calcareous plankton of the Campo Section
527 (Pyrenees, Spain): *Marine Micropaleontology*, v. 2001, no. 41, p. 45-71.

528 Patterson, W. P., and Walter, L. M., 1994, Depletion of ^{13}C in seawater CO_2 on modern carbonate
529 platforms: Significance for the carbon isotopic record of carbonates: *Geology*, v. 22, p. 885-888.

530 Pujalte, V., Baceta, J.I., Schmitz, B., 2015. A massive input of coarse-grained siliciclastics in the
531 Pyrenean Basin during the PETM: the missing ingredient in a coeval abrupt change in
532 hydrological regime. *Climate of the Past*, v. 11, no. 12, p. 1653-1672..

533 Pujalte, V., Orue-Etxebarria, X., Schmitz, B., Tosquella, J., Baceta, J. I., Payros, A., Bernaola, G.,
534 Caballero, F., and Apellaniz, E., 2003, Basal Ilerdian (earliest Eocene) turnover of larger
535 foraminifera: Age constraints based on calcareous plankton and $\delta^{13}\text{C}$ isotopic profiles from new
536 southern Pyrenean sections (Spain): *Geological Society of America Special Paper*, v. 369.

537 Pujalte, V., Robador, A., Payros, A., Sams , J.M., 2016. A siliciclastic braid delta within a lower
538 Paleogene carbonate platform (Ordesa-Monte Perdido National Park, southern Pyrenees, Spain):
539 Record of the Paleocene–Eocene Thermal Maximum perturbation. *Palaeogeography,
540 Palaeoclimatology, Palaeoecology*, v. 459, p. 453-470.

541 Pujalte, V., Schmitz, B., Baceta, J. I., Orue-Etxebarria, X., Bernaola, G., Turell, J. D., Payros, A.,

542 Apellaniz, E., and Caballero, F., 2009, Correlation of the Thanetian-Ilerdian turnover of larger
543 foraminifera and the Paleocene-ocene thermal maximum:confirming evidence from the Campo
544 area (Pyrenees, Spain): *Geologica Acta*, v. 7, no. 1-2, p. 161-175.

545 Pujalte, V., Schmitz, B., Baceta, J.I., 2014. Sea-level changes across the Paleocene–Eocene interval in
546 the Spanish Pyrenees, and their possible relationship with North Atlantic magmatism.
547 *Palaeogeography, Palaeoclimatology, Palaeoecology*, v. 393, p. 45-60.

548 Robinson, S.A., 2011. Shallow-water carbonate record of the Paleocene-Eocene Thermal Maximum
549 from a Pacific Ocean guyot. *Geology* 39, 51-54.

550 Röhl, U., Westerhold, T., Bralower, T. J., and Zachos, J. C., 2007, On the duration of the
551 Paleocene-Eocene thermal maximum (PETM): *Geochemistry, Geophysics, Geosystems*, v. 8, no.
552 12, p. 1-13.

553 Sanders, D., 2003, Syndepositional dissolution of calcium carbonate in neritic carbonate environments:
554 geological recognition, processes, potential significance: *Journal of African Earth Sciences*, v. 36,
555 no. 3, p. 99-134.

556 Scheibner, C., and Speijer, R. P., 2009, Recalibration of the Tethyan shallow-benthic zonation across
557 the Paleocene-Eocene boundary: the Egyptian record: *Geologica Acta*, v. 7, no. 1-2, p. 195-214.

558 Scheibner, C., Speijer, R.P., Marzouk, A.M., 2005. Turnover of larger foraminifera during the
559 Paleocene-Eocene Thermal Maximum and paleoclimatic control on the evolution of platform
560 ecosystems. *Geology*, v. 33, 493-496.

561 Sciunnach, D., Garzanti, E., 2012. Subsidence history of the Tethys Himalaya. *Earth Science Reviews*,
562 v. 111, 179-198.

563 Serra-Kiel, J., Hottinger, L., Caus, E., Drobne, K., Ferrandez, C., Jauhri, A.K., Less, G., Pavlovec, R.,
564 Pignatti, J., Samsó, M.J., Schaub, H., Sirel, E., Strougo, A., Tambaregu, Y., Tosquella, J.,
565 Zakrevskaya, E., 1998. Larger foraminifera biostratigraphy of the Tethyan Paleocene and Eocene.
566 *Bull. Soc. géol. France*, v. 169, no.2, p. 281–299.

567 Sluijs, A., and Dickens, G. R., 2012, Assessing offsets between the delta C-13 of sedimentary
568 components and the global exogenic carbon pool across early Paleogene carbon cycle
569 perturbations: *Global Biogeochemical Cycles*, v. 26.

570 Sluijs, A., Brinkhuis, H., Crouch, E. M., John, C. M., Handley, L., Munsterman, D., and Pancost, R. D.

571 2008, Eustatic variations during the Paleocene–Eocene greenhouse world, *Paleoceanography*,
572 23(4), PA4216, doi:10.1029/2008PA001615.

573 Sluijs, A., G. J. Bowen, H. Brinkhuis, L. J. Lourens, and E. Thomas, 2007. The Palaeocene–Eocene
574 thermal maximum super greenhouse: Biotic and geochemical signatures, age models and
575 mechanisms of global change, in *Deep Time Perspectives on Climate Change: Marrying the
576 Signal From Computer Models and Biological Proxies*, edited by M. Williams et al., pp. 323–347,
577 Geol. Soc., London.

578 Sluijs, A., Schouten, S., Pagani, M., Woltering, M., Brinkhuis, H., Damsté, J. S. S., Dickens, G. R.,
579 Huber, M., Reichert, G.-J., Stein, R., Matthiessen, J., Lourens, L. J., Pedentchouk, N., Backman,
580 J., Moran, K., and the Expedition, S., 2006, Subtropical Arctic Ocean temperatures during the
581 Palaeocene/Eocene thermal maximum: *Nature*, v. 441, no. 7093, p. 610-613.

582 Speijer, R. P., and Wagner, T., 2002, Sea-level changes and black shales associated with the late
583 Paleocene thermal maximum: Organic-geochemical and micropaleontologic evidence from the
584 southern Tethyan margin (Egypt-Israel): *Geological Society of America Special Paper*.

585 Speijer, R. P., Scheibner, C., Stassen, P., Abdel-Mohsen, and Morsi, M., 2012, Response of marine
586 ecosystems to deep-time global warming: a synthesis of biotic patterns across the
587 Paleocene-Eocene thermal maximum (PETM): *Austrian Journal of Earth Sciences*, v. 105, p. 6-16.

588 Strong, N. and Paola, C., 2008. Valleys that never were: time surfaces versus stratigraphic surfaces, *J.*
589 *Sediment. Res.*, v 78, p. 579–593

590 Swart, P. K., and Eberli, G., 2005, The nature of the $\delta^{13}\text{C}$ of periplatform sediments: Implications for
591 stratigraphy and the global carbon cycle: *Sedimentary Geology*, v. 175, no. 1-4, p. 115-129.

592 Van Hinsbergen, D. J., Lippert, P. C., Dupont-Nivet, G., McQuarrie, N., Doubrovine, P. V., Spakman,
593 W., & Torsvik, T. H., 2012. Greater India Basin hypothesis and a two-stage Cenozoic collision
594 between India and Asia. *Proceedings of the National Academy of Sciences*, 109(20), 7659-7664.

595 van Hinsbergen, D. J., Steinberger, B., Doubrovine, P. V., and Gassmüller, R., 2011. Acceleration and
596 deceleration of India - Asia convergence since the Cretaceous: Roles of mantle plumes and
597 continental collision. *Journal of Geophysical Research: Solid Earth*, 116(B6).

598 Wan, X.Q., Jansa, L.F., Sarti, M., 2002. Cretaceous-Paleogene boundary strata in southern Tibet and
599 their implication for the India-Eurasia collision. *Lethaia*, 35(2): 131-146.

600 Wang, X., Wan X. Q. and Li, G. B., 2010. Turnover of larger benthic foraminifera during the
601 Paleocene-Eocene stratigraphic boundary in Gamba, Tibet. *Acta Micropalaeontologica Sinica*, v.
602 27, no. 2, p. 109- 117.

603 Wendler, J. E., and Wendler, I., 2016, What drove sea-level fluctuations during the mid-Cretaceous
604 greenhouse climate?: *Palaeogeography, Palaeoclimatology, Palaeoecology*, v. 441, p. 412-419.

605 Westerhold, T., Röhl, U., and Laskar, J., 2012,. Time scale controversy: Accurate orbital calibration of
606 the early Paleogene: *Geochemistry, Geophysics, Geosystems*, v. 13, no. 6, p. n/a-n/a.

607 Willems, H., Zhang, B., 1993. Cretaceous and Lower Tertiary sediments of the Tibetan Tethys
608 Himalaya in the area of Gamba (South Tibet, PR Chian). *Berichte, Fachbereich Geowis-
609 senschaften, Universitat Bremen*, 38: 3-27.

610 Willems, H., Zhou, Z., Zhang, B., and Gräfe, K.-U., 1996, Stratigraphy of the Upper Cretaceous and
611 Lower Tertiary strata in the Tethyan Himalayas of Tibet (Tingri area, China): *Geol Rundsch* v. 85,
612 p. 723-754.

613 Wu, F. Y., Ji, W. Q., Wang, J. G., Liu, C. Z., Chung, S. L., and Clift, P. D., 2014,. Zircon U-Pb and Hf
614 isotopic constraints on the onset time of India-Asia collision: *American Journal of Science*, v. 314,
615 no. 2, p. 548-579.

616 Yi, Z., Huang, B., Chen, J., Chen, L., and Wang, H., 2011,. Paleomagnetism of early Paleogene marine
617 sediments in southern Tibet, China: Implications to onset of the India–Asia collision and size of
618 Greater India: *Earth and Planetary Science Letters*.

619 Zachos, J., Pagani, M., Sloan, L., Thomas, E., and Billups, K., 2001,. Trends, Rhythms, and
620 Aberrations in Global Climate 65 Ma to Present: *Science*, v. 292, no. 5517, p. 686-693.

621 Zamagni, J., Mutti, M., and Košir, A., 2012,. The evolution of mid Paleocene-early Eocene coral
622 communities: How to survive during rapid global warming: *Palaeogeography, Palaeoclimatology,
623 Palaeoecology*, v. 317-318, p. 48-65.

624 Zamagni, J., Mutti, M., Košir, A., 2008. Evolution of shallow benthic communities during the Late
625 Paleocene–earliest Eocene transition in the Northern Tethys (SW Slovenia). *Facies*, 54(1), 25-43.

626 Zhang, Q., Willems, H., Ding, L., 2013. Evolution of the Paleocene-Early Eocene larger benthic
627 foraminifera in the Tethyan Himalaya of Tibet, China. *Int J Earth Sci* 102, 1427-1445.

628 Zhang, Q., Willems, H., Ding, L., Gräfe, K.-U., and Appel, E., 2012,. Initial India-Asia

629 Continental Collision and Foreland Basin Evolution in the Tethyan Himalaya of Tibet: Evidence
630 from Stratigraphy and Paleontology: *The Journal of Geology*, v. 120, no. 2, p. 175-189.

631 **Figure captions**

632 Fig. 1: A) Schematic geologic map of the Himalayan Range; B) Geologic maps of the Gamba area,
633 showing the location of the studied sections.

634

635 Fig. 2: Field photographs: (A) Member 3, conglomerate bed, and member 4 of the Zongpu
636 Formation in the Zengbudong section, Gamba area; (B) nodular marly limestones of uppermost
637 member 3; (C) the conglomerate bed in the Zongpu Formation, Gamba area; (D) thick- and
638 massively-bedded limestones of member 4.

639

640 Fig. 3: Lithological log of the Zongpu Formation (Zongpu and Zengbudong sections) spanning the
641 Paleocene/Eocene boundary, showing the distribution of larger benthic foraminifera, carbonate
642 microfacies, interpreted palaeowater depths and depositional environments, and the distribution of
643 larger benthic foraminifera in carbonate clasts of the conglomerate bed. A) Floatstone with
644 *Alveolina* and *Orbitolites* in lowermost member 4; B) packstone with nummulitids in the
645 carbonate clasts, from the conglomerate bed; C) packstone with nummulitids in uppermost
646 member 3. SBZ = Shallow Benthic Zonation of Serra-Kiel et al., 1998; FWWB = fair-weather
647 wave base. Data from Li et al. (2015).

648

649 Fig. 4: Integrated chrono- and biostratigraphic framework for the Gamba sections of the southern
650 Tethyan Himalaya. Planktonic foraminiferal biozones from BouDagher-Fadel (2013); larger
651 benthic foraminiferal biozones from BouDagher-Fadel (2008, 2015). Timescale is based on
652 Gradstein et al. (2012). Legend corresponds to that in Fig. 3.

653

654 Fig. 5: Larger benthic foraminifera of SBZ4 through SBZ6 in the Zongpu and Zengbudong
655 sections. A) *Daviesina langhami*, Thanetian, SBZ4, 12ZP133; B) *Orbitosiphon punjabensis*,
656 Thanetian, SBZ4, 12ZP133; C) a. *Ranikothalia sindensis*, b. *Orbitosiphon praepunjabensis*

657 Adams, c. *Miscellanea juliettae*, d. *Lockhartia roeae*, Thanetian, SBZ4, 12ZP182; D) *Miscellanea*
658 *juliettae*, Thanetian, SBZ4, 12ZP182; E) *Miscellanea yvettae*, Thanetian, SBZ4, 12ZP229; F) a.
659 *Orbitolites complanatus*, b. *Alveolina ellipsoidalis*, Ypresian, later part of SBZ6, 13ZB72; G) a.
660 *Orbitosiphon punjabensis*, b. *Lockhartia conditi*, c. *Miscellanea miscella*, d. *Lockhartia diversa*,
661 reworked late Thanetian SBZ4 assemblage mixed with early Ypresian assemblage, 12ZD69; H)
662 *Alveolina ellipsoidalis* and *Alveolina pasticillata*, Ypresian, late SBZ6, 13ZB72.

663

664 Fig. 6: Lithostratigraphy, biostratigraphic ranges of larger benthic foraminifera, and whole-rock
665 carbonate $\delta^{13}\text{C}$ curve for the Zongpu section, Gamba area. SBZ= Shallow Benthic Zone,
666 TP=Tibetan Foraminiferal Biozone, CIE= Carbon Isotopic Excursion; M= mudstone; W=
667 wackestone; P= packstone; G= grainstone; F= floatstone. Legend corresponds to that in Fig. 3.

668

669 Fig. 7: Lithostratigraphy, biostratigraphic ranges of larger benthic foraminifera, and $\delta^{13}\text{C}$ curves
670 for whole-rock carbonate and organic matter from the Zengbudong section, Gamba area.

671

672 Fig. 8: Crossplots of: A) Whole-rock carbonate carbon versus oxygen isotopes ($\delta^{13}\text{C}$ vs. $\delta^{18}\text{O}$)
673 from the Zongpu Formation, in the Zongpu and Zengbudong sections; B) Whole-rock carbonate
674 carbon versus organic carbon isotopes ($\delta^{13}\text{C}_{\text{carb}}$ vs. $\delta^{13}\text{C}_{\text{org}}$) of carbonate clasts from the
675 conglomerate bed in the Zengbudong section.

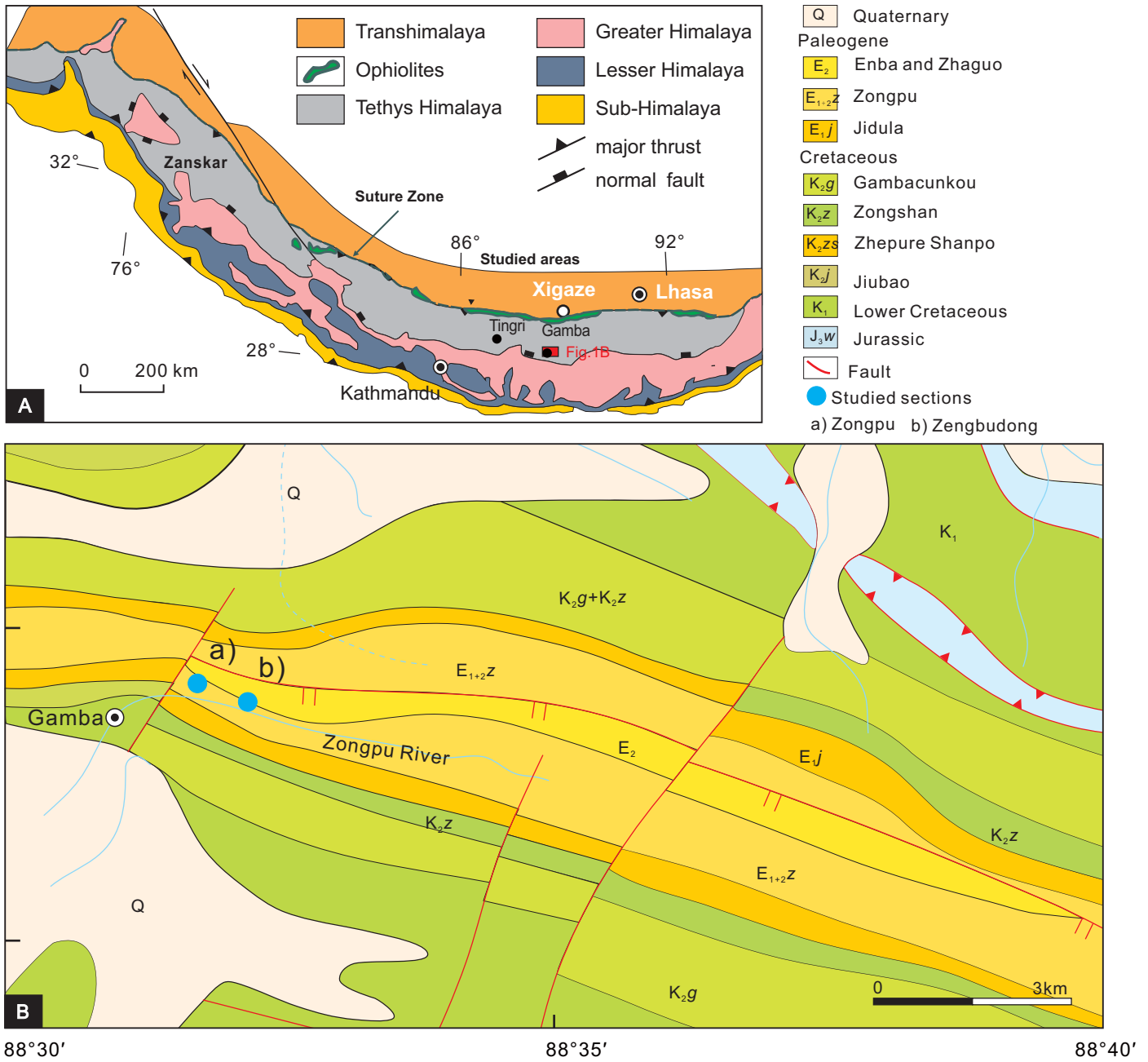
676

677 Fig. 9: Integrated field photography, lithological log, and stable isotope curve from the
678 Zengbudong section, spanning the Paleocene/Eocene boundary in the Gamba area, southern Tibet.

679

680 Fig. 10: Chemostratigraphic correlation of PETM records based on stable carbon isotopes, from
681 the Gamba area of southern Tibet (this study), Kozina, SW Slovenia ([Zamagni et al., 2012](#)), and
682 the Southern Ocean (ODP690; [Kennett et al., 1991](#)).

Figure



Li et al., Fig.1

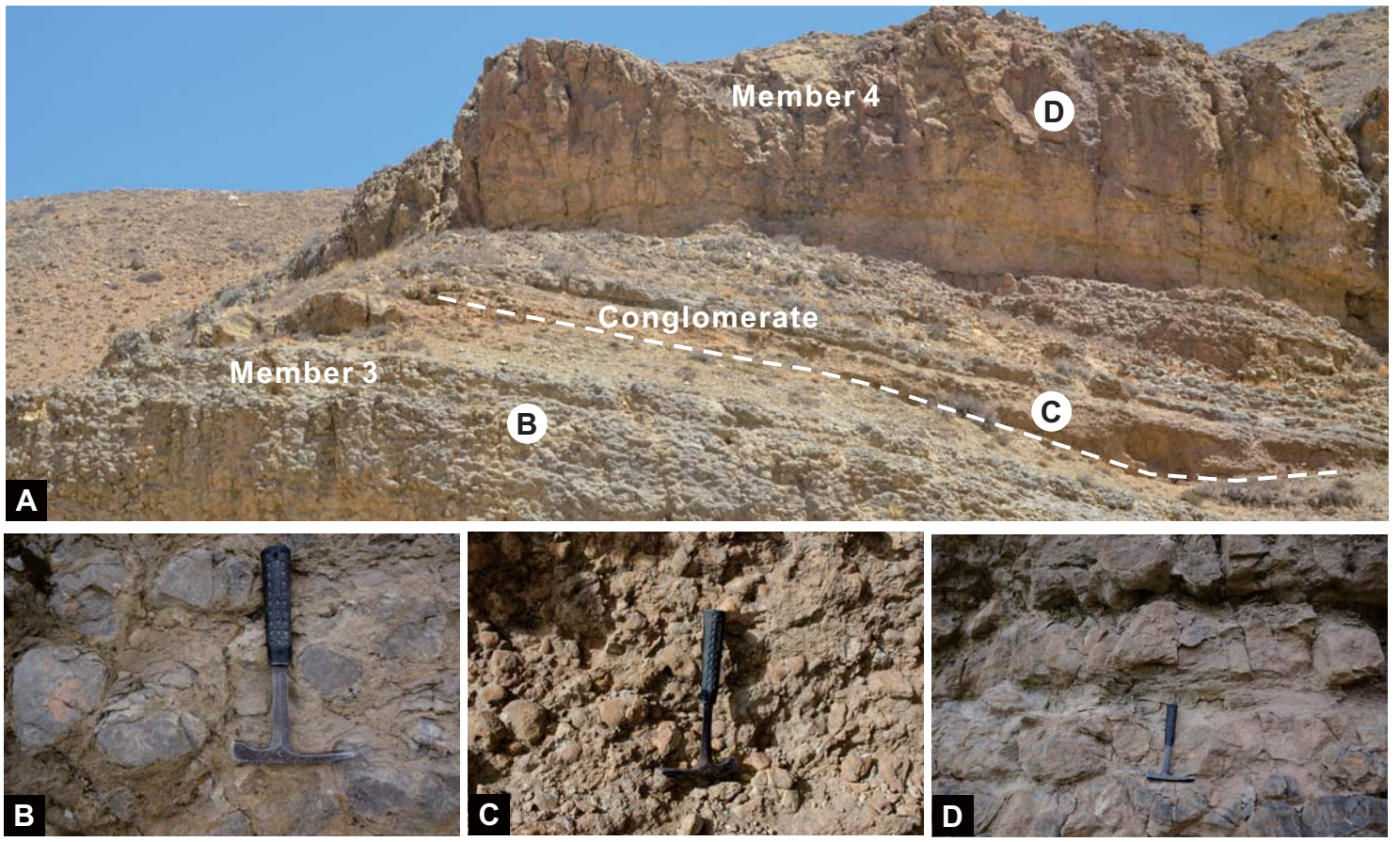
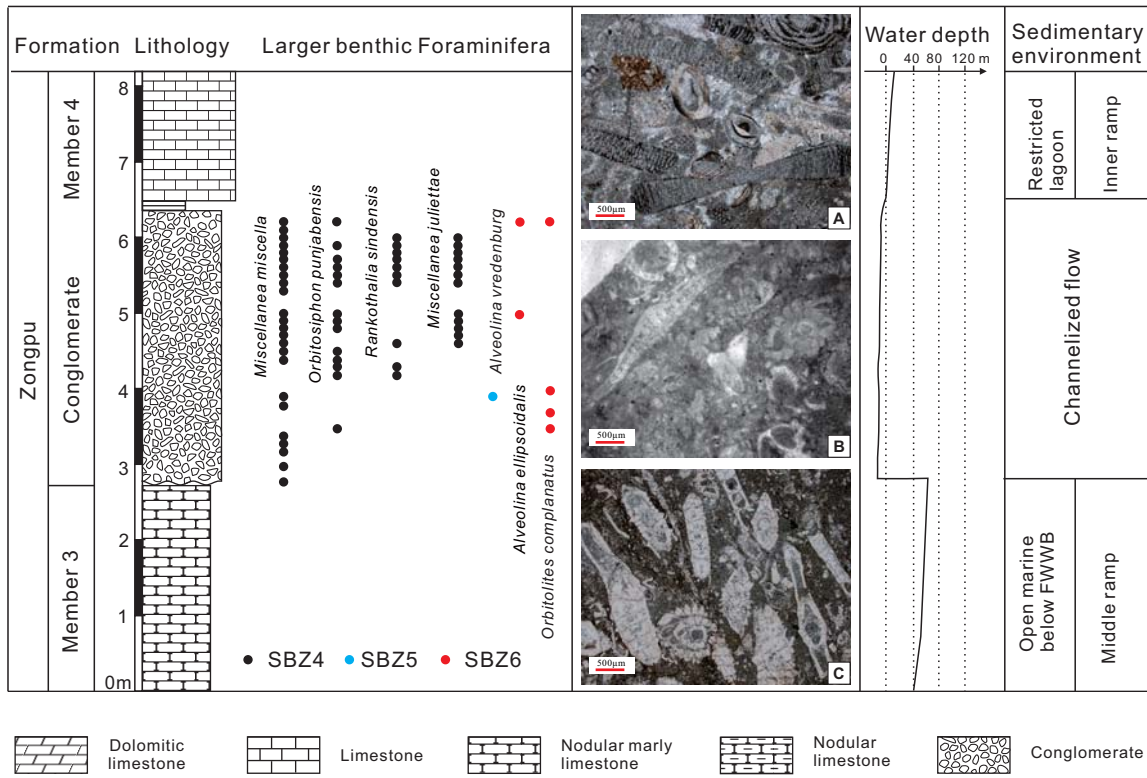


Fig. 2 Li et al.



Li et al., Fig. 3

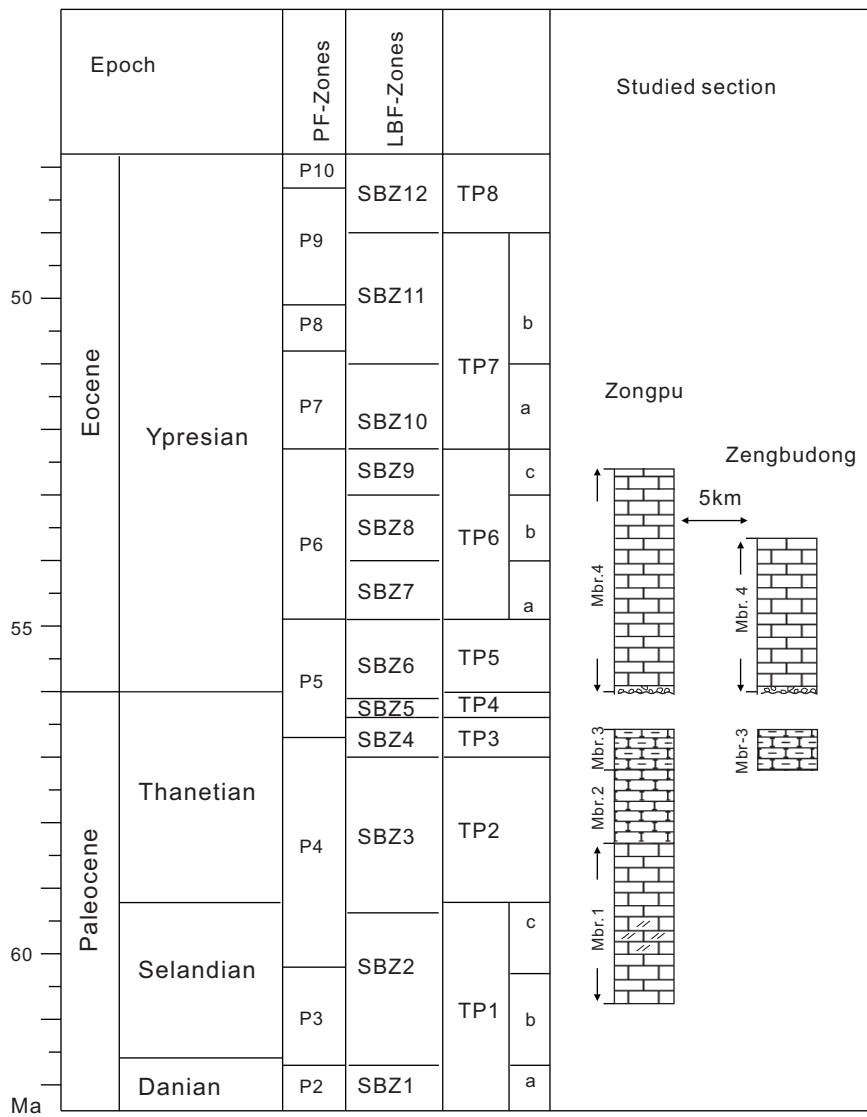


Fig. 4

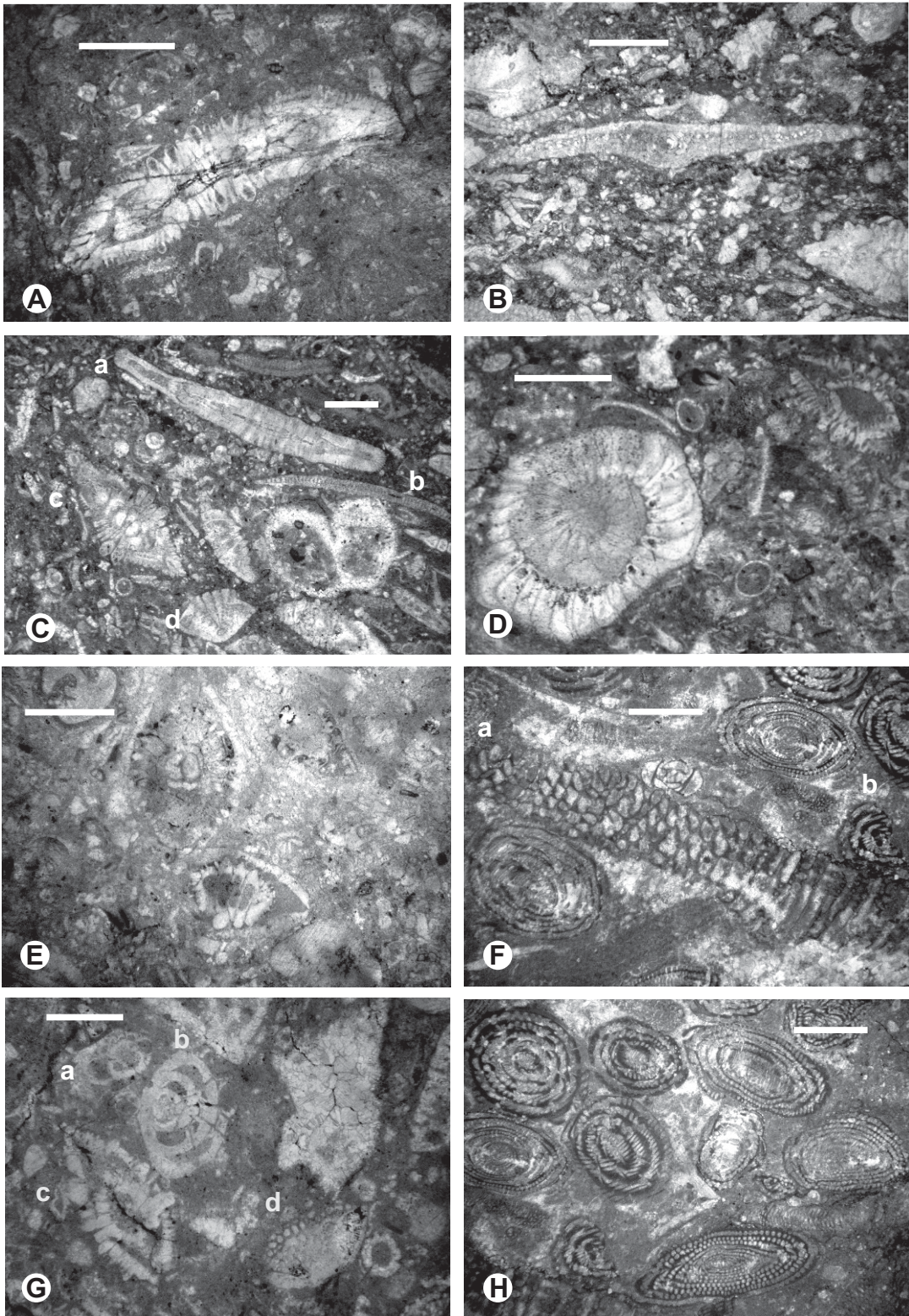


Fig. 5

Zongpu Section, Gamba

Paleocene		Eocene	
Danian	Selandian	Ypresian	Epoch
Thanetian		Member	Stage
1		4	4
TP2	TP3	TP5	TP6
SBZ3	SBZ4	SBZ6	SBZ7
SBZ2		SBZ8	SBZ9
SBZ1			

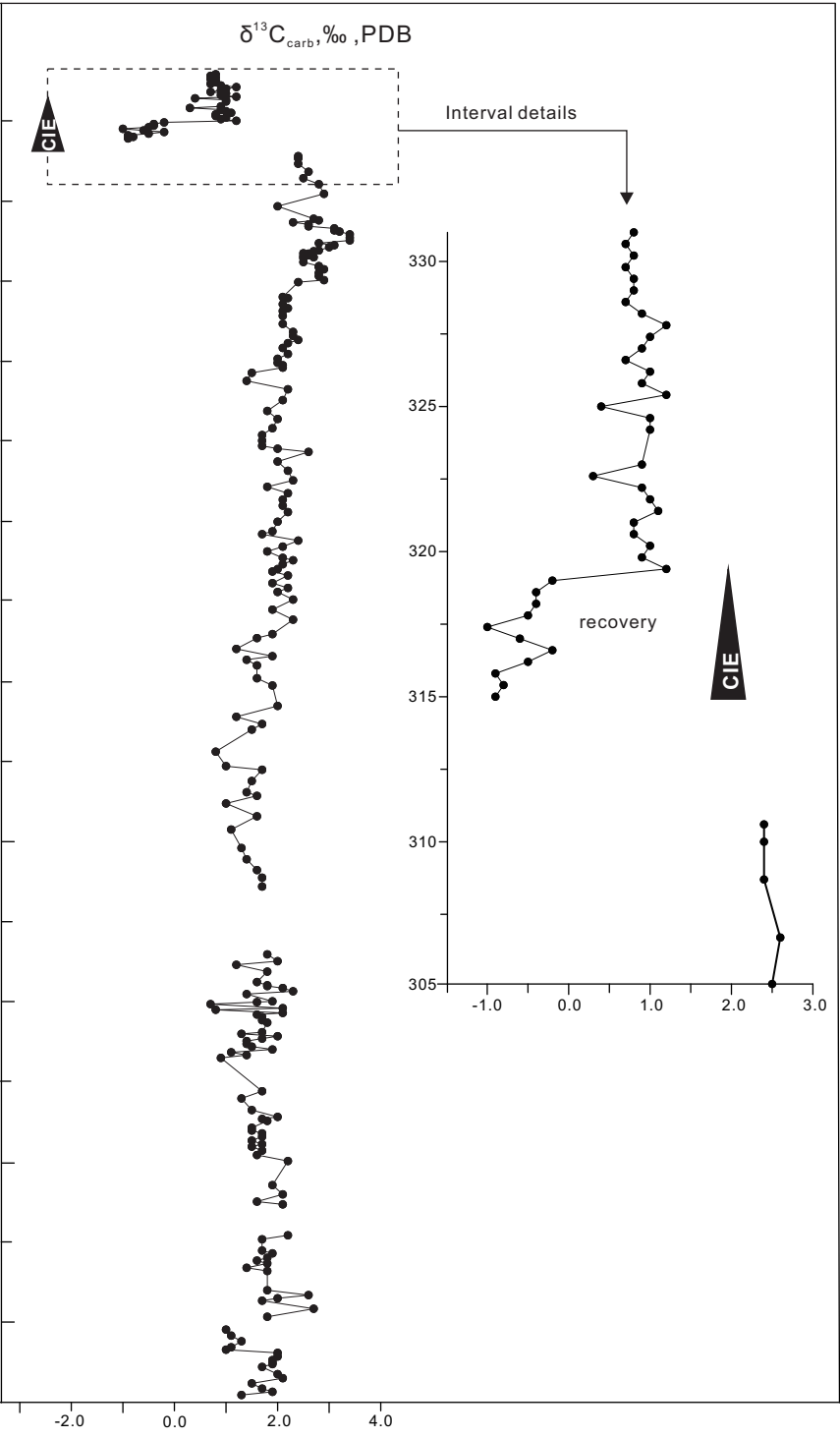
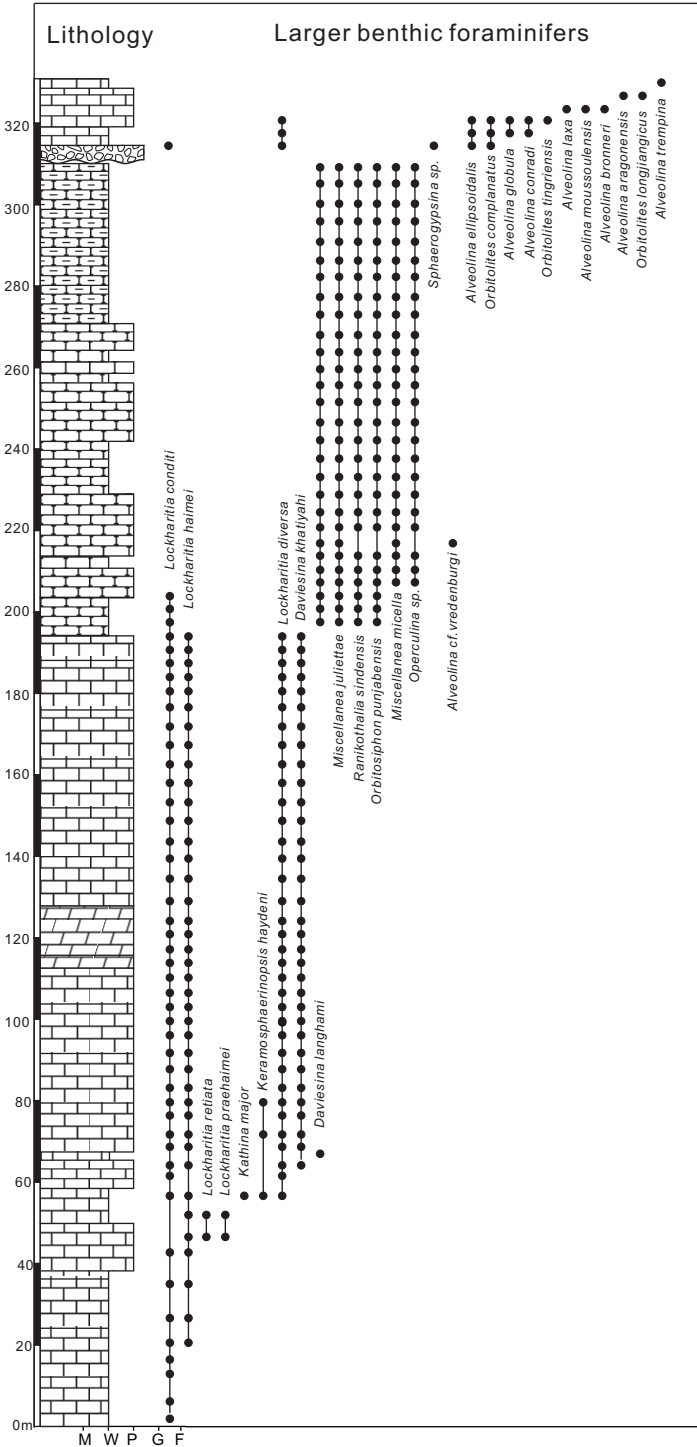


Fig.6

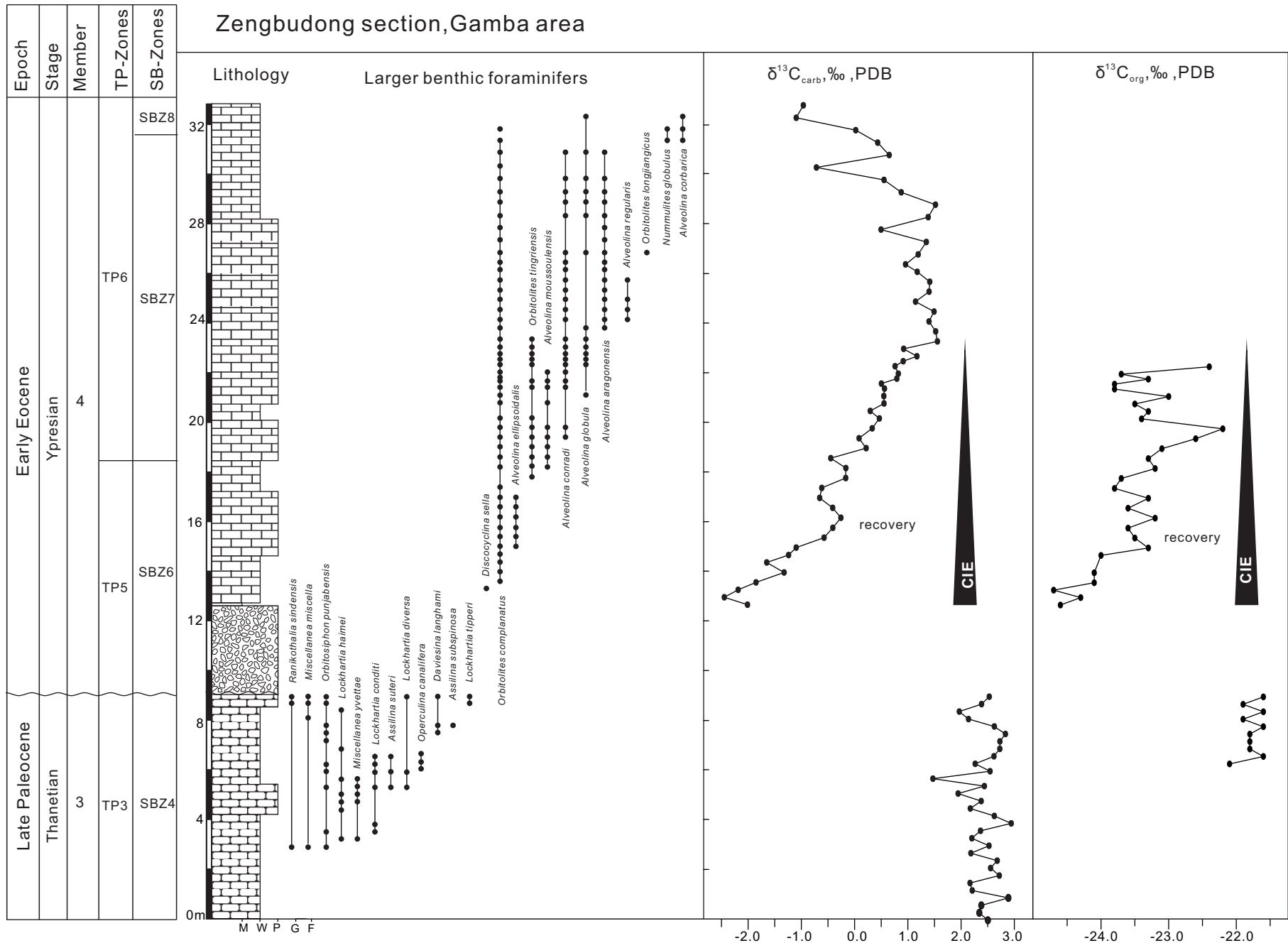


Fig. 7

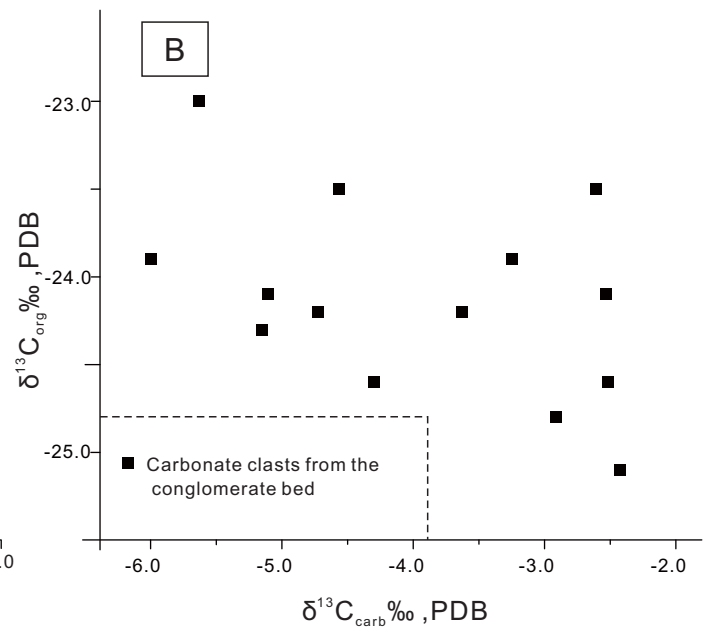
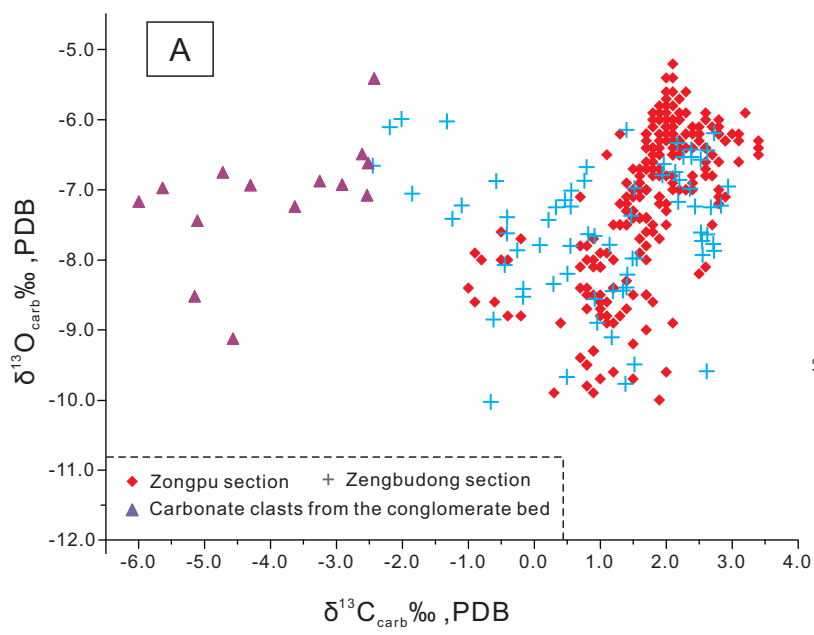


Fig.8

Zengbudong section

Field view of the conglomerate directly overlying the member 3

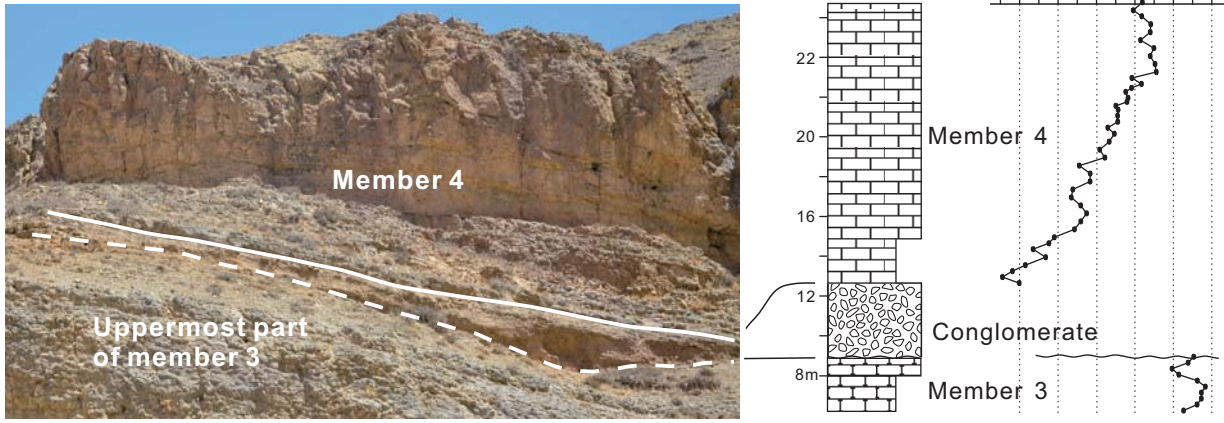
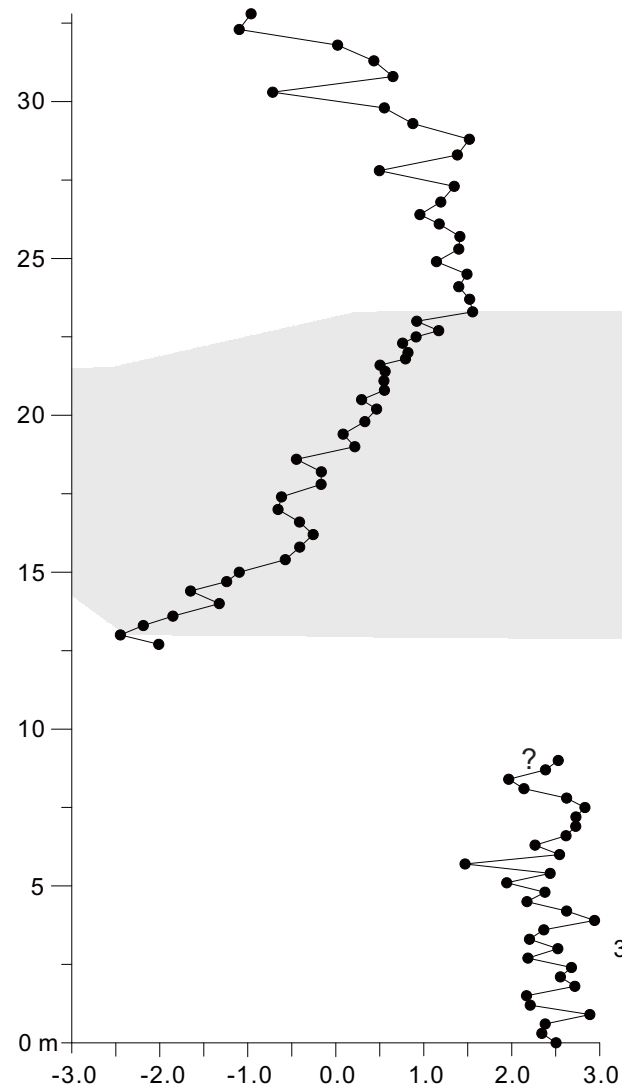
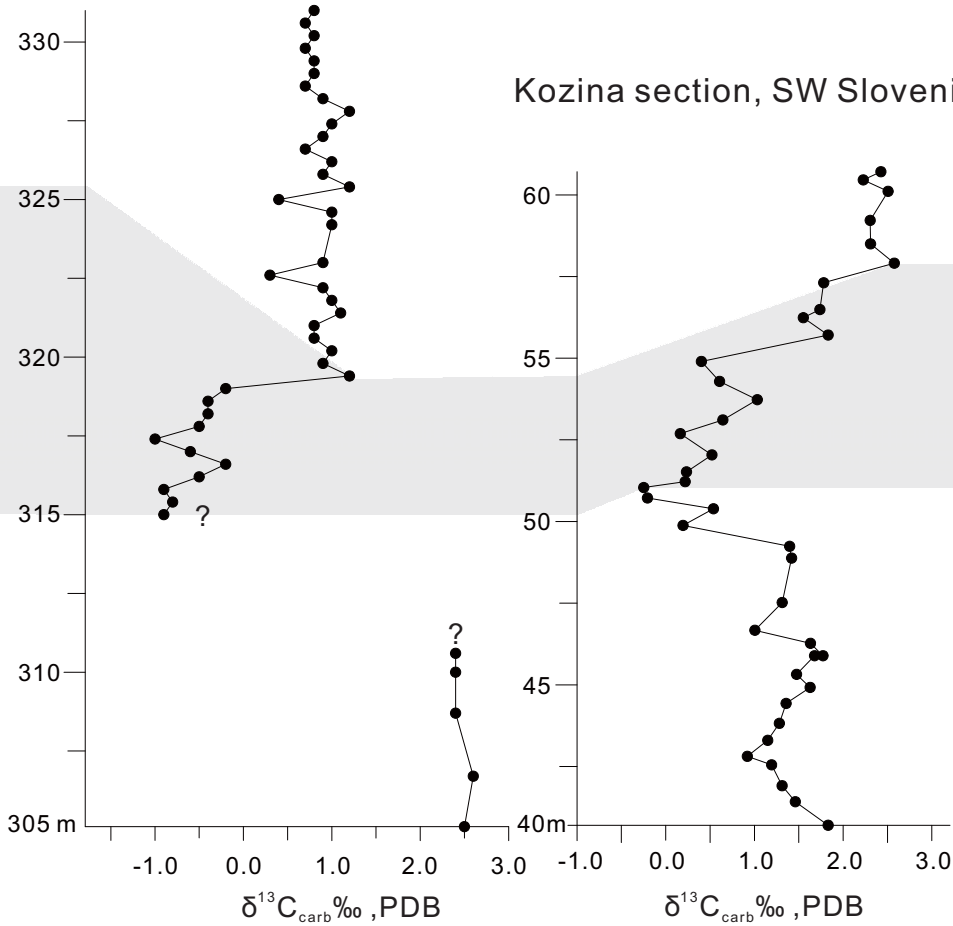


Fig. 9

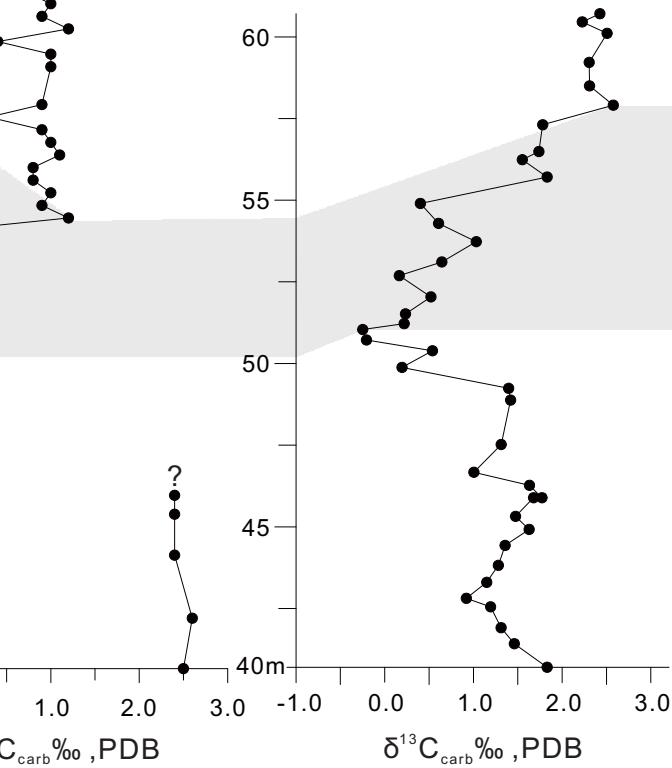
Zengbudong section, Gamba (Southern Tibet)



Zongpu section, Gamba (Southern Tibet)



Kozina section, SW Slovenia



ODP690, South Ocean

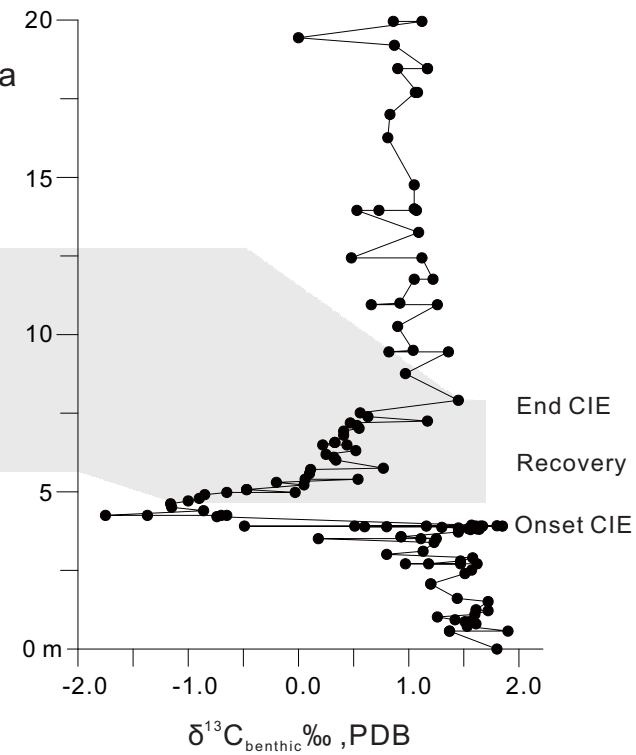


Fig. 10 $\delta^{13}\text{C}_{\text{carb}}$ ‰, PDB



南京大學
NANJING UNIVERSITY

School of Earth Sciences
22 Hankou Road, Nanjing, P. R. China
Tel: 86 25 89683002 Fax: 86 25 83686016
<http://www.nju.edu.cn>

June 11, 2016

Dear Editor (*Palaeogeography, Palaeoclimatology, Palaeoecology*),

We would like to submit our original article entitled “**Shallow-water carbonate response to the Paleocene–Eocene thermal maximum in the Tethys Himalaya (southern Tibet): tectonic and climatic implications**” for publication.

This manuscript is entirely original and not submitted elsewhere for publication. If accepted, we are willing to pay the extra charge for color figures.

For potential referees, we would like to recommend the following researchers, who are familiar with Paleocene–Eocene thermal maximum and Tethyan Himalaya geology.

Dr. Helmut Weissert, ETH Zurich, Switzerland, Email: helmut.weissert@erdw.ethz.ch

Dr. Appy Sluijs, Utrecht University, Netherlands; Email: a.sluijs@uu.nl

Dr. Qinghai Zhang, University of Bremen, Germany; Email: zhang@uni-bremen.de

Dr. Xiaojiao Wan, China University of Geosciences, Beijing; Email: [wanxq@cugb.edu.cn](mailto:wanaxq@cugb.edu.cn)

Dr. Victoriano Pujalte, University of the Basque Country, Spain; Email: victoriano.pujalte@ehu.es

We thank you for your kind consideration, and look forward to hearing from you in due course.

Sincerely yours,

Xiumian Hu (Corresponding author, huxm@nju.edu.cn)

Juan Li, Xiumian Hu*, Eduardo Garzanti, Marcelle BouDagher-Fadel

Supplementary Interactive Plot Data (CSV)

[Click here to download Supplementary Interactive Plot Data \(CSV\): Appendix.xls](#)